THE EUROPEAN PHYSICAL JOURNAL C

NuTag: a proof-of-concept study for a long-baseline neutrino beam

A. Baratto-Roldán[1,a] [ORCID]**, M. Perrin-Terrin[2], E. G. Parozzi[1], M. A. Jebramcik[1], N. Charitonidis[1]**

[1] CERN, BE Department, Esplanade des Particules 1, Meyrin, 1211 Geneva 23, Switzerland
[2] Aix Marseille Univ, CNRS/IN2P3, CPPM, Marseille, France

Abstract The study of neutrino oscillation at accelerators is limited by systematic uncertainties, in particular on the neutrino flux, cross section, and energy estimates. These systematic uncertainties could be eliminated by a novel experimental technique: neutrino tagging. This technique relies on a new type of neutrino beamline and its associated instrumentation which would enable the kinematic reconstruction of the neutrinos produced in $\pi^{\pm} \to \mu^{\pm} \overset{\leftrightarrow}{\nu}_{\mu}$ and $K^{\pm} \to \mu^{\pm} \overset{\leftrightarrow}{\nu}_{\mu}$ decays. This article presents a proof-of-concept study for such a tagged beamline, aiming to serve a long-baseline neutrino experiment exploiting a megaton scale natural water Cherenkov detector. After optimising the target and the beamline optics to first order, a complete Monte Carlo simulation of the beamline has been performed. The results show that the beamline provides a meson beam compatible with the operation of the spectrometer, and delivers a neutrino flux sufficient to collect neutrino samples with a size comparable with similar experiments and with other un-tagged long-baseline neutrino experimental proposals.

1 Introduction

Neutrino tagging is a novel technique being developed for accelerator-based neutrino experiments [1]. Usually, the characteristics of the neutrinos (energy, flavour, direction, and chirality) are estimated based on the signals they induce when interacting in a neutrino detector. The properties of these interacting neutrinos are then used to infer the overall neutrino flux, which is essential to study neutrino oscillations. However, as only a tiny fraction of neutrinos interacts with the detector, the flux calculation is limited by large uncertainties. In addition, the precision on the expected neutrino characteristics is strongly limited by the uncertainties in the models describing the neutrino interactions. While the

neutrino oscillations studies could so far accommodate these uncertainties, they are becoming the limiting factor for the physics program of the next generations of experiments [2–4].

The neutrino tagging (NuTag) technique [1] proposes to exploit the neutrino production mechanisms to complement the information obtained using the interactions in neutrino detectors. While neutrinos can interact with matter through multiple interaction channels, all exhibiting large experimental signature variability [5], their production mechanisms are dominated by two experimentally well controlled processes: the $\pi^{\pm} \to \mu^{\pm} \overset{\leftrightarrow}{\nu}_{\mu}$ and the $K^{\pm} \to \mu^{\pm} \overset{\leftrightarrow}{\nu}_{\mu}$ decays. Hence, the neutrinos can be kinematically reconstructed from the $\pi^{\pm}$ and $\mu^{\pm}$ or $K^{\pm}$ and $\mu^{\pm}$ characteristics. With these particles being electrically charged, they can be detected with high efficiency and precision [6]. The neutrinos reconstructed as such are called *tagged neutrinos*. This reconstruction method offers unmatched precision on the neutrino characteristics. For example, neutrino energy resolutions better than 1% [1] can be obtained with the tagging, while the typical energy resolutions of neutrino detectors are of the order of 10–30% [7,8]. Moreover, as elaborated in Ref. [1], the resolution on the direction and time of arrival of the tagged neutrinos allows each interacting neutrino to be associated with its corresponding tagged neutrino. As a result, a tagged neutrino experiment can exploit the precise information provided by the tagging to study a wide range of topics both at short- and long-baseline experiments, such as neutrino interaction models and cross sections or, neutrino oscillations. The former two are crucial inputs for the upcoming long-baseline experiments [9], Deep Underground Neutrino Experiment (DUNE [10]) and Tokai-to-Hyper-Kamiokande (T2HK [8]). For the latter, preliminary studies [1] indicate that a tagged neutrino beam with a $\mathcal{O}$(Mton) scale natural-water Cherenkov detector would reach unmatched precision on the phase controlling the charge-parity violation in the neutrino sector δ_{CP}.

[a] e-mail: anna.baratto.roldan@cern.ch (corresponding author)

Springer

More details on the sensitivity study (e.g. energy resolution, background suppression) are available in Ref. [1].

The concept of neutrino tagging was originally introduced in the 1970s with various experimental proposals [11–18]. Despite their differences, all these designs relied on instrumenting the beamline to detect the meson's decay products and, ideally, the mesons themselves. Among these designs, only one has been implemented: the Tagged Neutrino Facility (TNF) [16] in Serpukhov that only featured instruments to characterise the mesons decay products. To the authors' best knowledge, the TNF collaboration has not published any results, except preliminary ones showing one neutrino in coincidence with a μ^+ [19].

In a tagged neutrino experiment, the neutrino rate is directly limited by the beam instrumentation performance (e.g. the readout capability or the time resolution) [12]. Such limitations probably hindered the development of the tagging technique and led the community to adopt experimental designs with maximum beam intensities towards the maximum number of neutrinos to be detected in the neutrino detectors. However, with the recent progress of silicon pixel technologies, the detection rate capability has significantly increased. The ongoing developments in the silicon pixel detector technology field [20–22] will allow readout fluxes as high as 100 MHz/mm^2, integrated fluences of 10^{16-17} n$_{eq}$/cm^2 and time resolutions as good as 10 ps [23]. In this context, our present work targets the design of a beamline specifically tailored to exploit the advantages of the NuTag technique.

In this article, we present a conceptual design for a tagged long-baseline neutrino beam for the study of neutrino oscillations. In tagged setups, as the one we propose, the neutrino initial flavour, chirality, energy, and direction are determined by the "tagger"(the devices identifying the parent meson's properties) with high precision. Thus, the purpose of the far detector is limited to the identification of the neutrinos' flavour. As a result, the granularity of the far detectors is not as crucial as for non-tagged experiments. Hence, an interesting option is to employ $\mathcal{O}$(Mton) scale natural-water Cherenkov detectors which can attain sizes two orders of magnitude larger than the detectors of the upcoming experiments (DUNE and T2HK). For example, KM3NeT-ORCA (Oscillation Research with Cosmics in the Abyss [24]), an experiment under construction off-shore of France, will ultimately instrument 6.8 Mton of sea water [25]. The energy threshold of this detector is 4 GeV [25]. In this paper, we have mainly considered the case study of an experiment with an energy of the first oscillation maximum ($E_1^{\text{vac.}}$)[1] at 5.0 GeV, which corresponds to a baseline length (BL) of 2600 km similar to P2O (Protvino to ORCA [27]). Since the

natural water Cherenkov detection technology developed for KM3NeT/ORCA [28] would allow access to both high and low energy ranges, with energies as low as 1 GeV [29], several other configurations could be envisaged such as:

- CERN to Pylos, Greece (BL of 1700 km – $E_1^{\text{vac.}}$ of 3.3 GeV) [30],
- CERN to Gulf of Taranto, Italy (BL of 1250 km – $E_1^{\text{vac.}}$ of 2.4 GeV) [31],
- CERN to Capo-Pasero KM3NeT-ARCA site (Astroparticle Research with Cosmics in the Abyss [24]), Italy (BL of 1300 km – $E_1^{\text{vac.}}$ of 2.5 GeV),
- European Spallation Source[2] to La Seyne-Sur-Mer (KM3NeT-ORCA site [24]), France (BL of 1500 km – $E_1^{\text{vac.}}$ of 2.9 GeV),
- Fermilab to the Northeast Pacific Time-Series Undersea Networked Experiments (NEPTUNE, BL of 3100 km – $E_1^{\text{vac.}}$ of 6.0 GeV) [32].

This next generation of tagged neutrino experiments can supersede the upcoming ones [8,10] only if they provide, (a) better control of the systematical uncertainties on the neutrino flux and energy estimate than the upcoming experiments and, (b) neutrino samples at least as large as those. While the tagging is expected to drastically reduce these systematic uncertainties, it will also limit the neutrino-beam rate which, convoluted with the detector mass, determines the neutrino sample size. Hence, in this work, we use the number of neutrino interactions, $n_{\overset{\leftrightarrow}{\nu}_e}$, as a figure of merit. This number can be expressed as

$$n_{\overset{\leftrightarrow}{\nu}_e}(E_1^{\text{mat.}}) = \mathcal{F}_{\overset{\leftrightarrow}{\nu}_\mu}(E_1^{\text{mat.}}) \cdot$$
$$\cdot P(\overset{\leftrightarrow}{\nu}_\mu \to \overset{\leftrightarrow}{\nu}_e)(E_1^{\text{mat.}}) \cdot \sigma_{\overset{\leftrightarrow}{\nu}_e}^{CC} \cdot \mathcal{N}_{\text{nucl}}, \qquad (1)$$
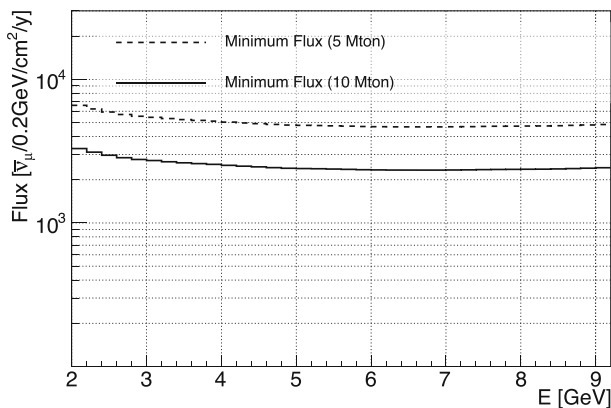
with $E_1^{\text{mat.}}$ the energy of the first oscillation maximum derived with the OscProb software [33] accounting for matter effects [34,35] and using the same oscillation parameters values as [10], $\mathcal{F}_{\overset{\leftrightarrow}{\nu}_\mu}$ the neutrino flux, $P(\overset{\leftrightarrow}{\nu}_\mu \to \overset{\leftrightarrow}{\nu}_e)$ the oscillation probability, $\sigma_{\overset{\leftrightarrow}{\nu}_e}^{CC}$ the charged current neutrino cross section and $\mathcal{N}_{nucl}$ the number of nucleons in the detector. The latter is obtained from the detector effective mass, the molar masses of its constitutive elements and the Avogadro's number. Hence, using Eq. (1) in combination with the number of oscillated $\overset{\leftrightarrow}{\nu}_e$ expected for DUNE at the first oscillation maximum [10], one can derive a minimum flux for a given detector mass and $E_1^{\text{mat.}}$. The minimum fluxes for a 5 and a 10 Mton detector are shown in Fig. 1. For neutrinos, both the oscillation probability and cross section increase with $E_1^{\text{mat.}}$. Hence, the minimum neutrino flux steadily decreases with $E_1^{\text{mat.}}$. In contrast, for anti-neutrinos, while the cross-section increases

---

[1] The $E_1^{\text{vac.}}$ is computed for neutrinos in vacuum and using oscillation parameter values from Ref. [26].

[2] Extra accelerating infrastructure would be needed to bring the protons to an energy sufficient to produce neutrinos at $E_1^{\text{vac.}}$.

E,
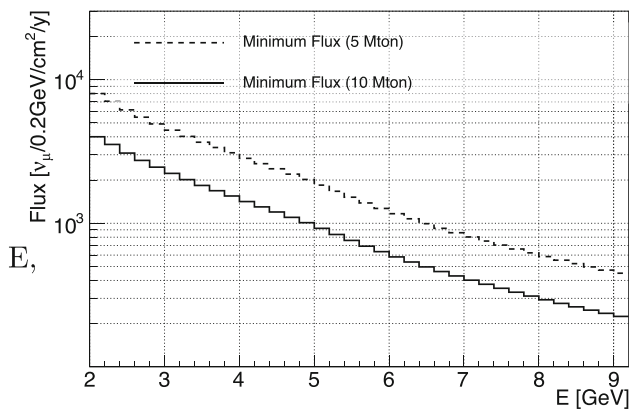
Fig. 1 Minimum neutrino (**a**) and anti-neutrino (**b**) fluxes required to collect neutrino samples as large as DUNE [10] assuming a 5 Mton and a 10 Mton far detectors. The fluxes are shown as a function of the energy of the first oscillation maximum, calculated accounting for matter effects [34,35] with the OscProb software [33]

with $E_1^{\mathrm{mat.}}$, the oscillation probability decreases with it. As a result, the minimum flux is constant above 3 GeV, as shown in Fig. 1b.

2 Neutrino beamline design general considerations

The first systematic studies on accelerator neutrino beams were presented in 1965 [36], where the definition of "conventional" neutrino beams, being used until today, was coined. In conventional neutrino beams, the neutrinos originate from the decay of $\pi^\pm$ or $K^\pm$ typically produced by the interaction of a high-intensity, high-momentum proton beam with target material. The $\pi^\pm \rightarrow \mu^\pm \overleftrightarrow{\nu}_\mu$ process dominates the $K^\pm \rightarrow \mu^\pm \overleftrightarrow{\nu}_\mu$ process in terms of quantity due to the smaller number of produced kaons. Also, the electron-neutrinos are always subdominant because they are created either by

$K^\pm \rightarrow e^\pm \pi^0 \nu_e$ ($\overline{\nu}_e$) or by the decay in flight of $\mu^\pm$, like $\pi^+ \rightarrow \mu^+ \nu_\mu \rightarrow (e^+ \nu_e \overline{\nu}_\mu) \nu_\mu$, both processes being rare.

The readers can find an extensive review of the design on accelerator neutrino beams in Ref. [37] and a more recent discussion in Ref. [38]. For historical reasons [39], the majority of the accelerator-driven systems for neutrino production are optimised for the maximum neutrino flux rather than for the precision on the knowledge of the neutrino momentum and rate. These "wide-band" beams compensate for the small interaction cross sections of the low-GeV/c scale neutrinos with a large flux.

The production of a wide (or narrow) band neutrino beam can be quite different depending on the physics scope of the experiment being served by it. However, in general, the following considerations must be taken into account in all cases:

– A high-intensity proton beam impinging on a target to produce the unstable neutrino parent particles is necessary. The primary beam must be of sufficiently high momentum and power so that a satisfactory number of secondary particles, i.e., pions and kaons, are produced [26]. The proton extraction on the target can be fast (of the order of a few ns), slow (above 700 ms) or fast-slow (of the order of 1 ms as in the now dismantled West Area Neutrino Facility [40] at CERN). The exact structure of the proton beam may have implications on the target lifetime and may require explicit cooling or special design considerations. If the beam is fast-extracted as was proposed in the case of the Neutrino Factory [41] for instance, then the target design becomes very challenging. Novel target concepts like tungsten powder [42,43] or liquid mercury [44] have been proposed as viable materials for such cases, with still many open questions and requiring dedicated research and development for a realistic implementation. Even in the case of slow-extracted beams, the radiation damage of the target material may become an important concern if integrated fluxes of the order of 10^{20} protons/cm^2 are delivered on the target (see for example [45]).

– Downstream of the target, a focusing section must be installed to transversely select a satisfactory fraction of the produced secondaries at the target. Typically, either quadrupole magnets or magnetic horns are employed, with their respective advantages or disadvantages (discussed extensively in Ref. [38]) and in conjunction with the selected extraction scheme. Most of the horns used or proposed worldwide are optimised for focusing a single charge polarity at a given time due to the toroidal field of the horn [46–48].

– If limiting the particle momentum is necessary for the parent hadrons, or if a specific central momentum of the parent hadron is required for the experimental scope, a
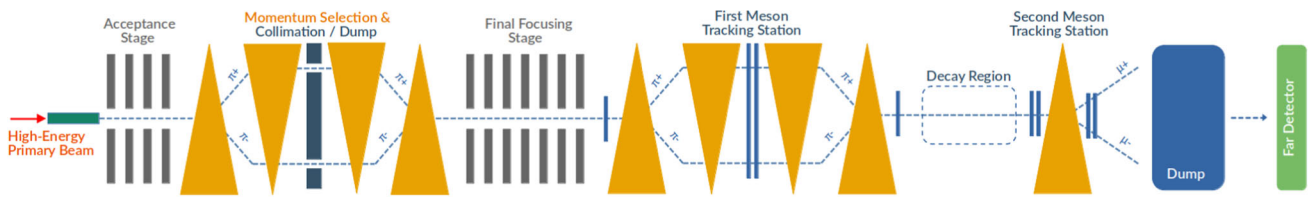
Fig. 2 Conceptual scheme of the proposed NuTag beamline. The high energy beam impinging on the target produces secondary particles (only the π^+ and π^- beams are shown for simplicity) that are subsequently focused, momentum selected and transported towards the meson tracking station. After their tagging at that point, the secondary beam continues straight towards a decay region where both π^+ and π^- will decay to neutrinos. Finally, a second spectrometer measures the momentum, direction and time of arrival of the $\mu^\pm$ from the decay, followed by a dump to absorb the remaining surviving beam particles

momentum-selection section of the hadron beamline is needed. Typically, this involves bending magnets and collimating slits. An example of this momentum-selection technique in the $p = 1$–7 GeV/c range is discussed in Refs. [49,50] for the H4-VLE beamline serving the NP-04 detector.

– The overall background imperatively needs to be minimised. The production of secondaries in the beamline's apertures at or downstream of the momentum selection, will create pions or muons that will subsequently decay to neutrinos of a different momentum, possibly reaching also the far detector and generating events that cannot be reconstructed. The largest challenge in this respect is the primary beam, which needs either to be dumped outside the axis of the neutrino trajectory or very early upstream in the line, ideally followed by bending magnets. Another argument for the background minimisation is the slow read-out rates of the neutrino detectors, e.g., the reader may refer to the novel NP-04 neutrino detector for the future DUNE experiment, with a readout rate of the order of a few Hz [51].

3 The NuTag beamline concept

A schematic of the proposed beamline concept is shown in Fig. 2. In the proposed beamline, a particle accelerator delivers a high-energy, high-intensity proton beam to a target. The secondary hadrons that are emitted by the target are subsequently focused and momentum selected within a very broad momentum range ($\delta p/p$ of the order of 25%), while the primary proton beam and all the neutral hadrons coming from the target are dumped onto the thick material between the openings of a collimating structure that acts as an effective primary beam dump integrated in a momentum slit. Then, the momentum, direction, and time of arrival of all beam particles are measured by a beam spectrometer made of four dipole magnets, interspaced with tracking stations and arranged to form an achromat [52]. These particles then drift in space (order of 900 m) where the majority will decay. At the end of

this drift space, a second spectrometer, made of two pairs of tracking stations installed before and after a large dipole magnet, measures the momentum, direction, and time of arrival of the decay products stemming from the beam particles, in particular the $\mu^\pm$'s from the $\pi^\pm \to \mu^\pm \overset{\leftrightarrow}{\nu}_\mu$ and $K^\pm \to \mu^\pm \overset{\leftrightarrow}{\nu}_\mu$ processes. The information provided by the two spectrometers combined allows the tagged neutrino's properties to be reconstructed based on the decay kinematics. The second spectrometer is followed by an absorber that stops the remaining surviving mesons before they decay. The length of the beamline section upstream of the first and downstream of the second spectrometer should be as short as possible to reduce the number of $\pi^\pm$ and $K^\pm$ decaying there since these cannot be reconstructed[3]. Finally, as the neutrino chirality is determined by the charge of the particles in the spectrometer, the hereby proposed NuTag technique does not require removing one of the two beam particle polarities. Hence, the beamline should ideally transport beam particles of both charges. Besides the obvious gain in terms of running time, collecting both neutrinos and antineutrinos simultaneously is a strong asset to reduce systematical uncertainties for key measurements such as δ_{CP}.

3.1 Proposed NuTag beamline layout

In order to satisfy the physics case discussed in the introduction, the beamline design is optimised for a long-baseline type of facility. The primary beam considered here is expected to be a slow-extracted, high-momentum proton beam. On one hand, the constraint on the maximum rate that is accepted by the tracking detectors (of the order of 10–100 MHz/mm^2) can only be achieved via a slow extraction. On the other

---

[3] To estimate the fraction of un-taggable neutrinos, one can conservatively assume that $\pi^\pm \to \mu^\pm \overset{\leftrightarrow}{\nu}_\mu$ decays occurring upstream of the tagger yield as many neutrinos in the far detector acceptance as the decays occurring downstream of it. Under this assumption, the fraction of un-taggable neutrinos is $(e^{d/\beta\gamma c\tau} - 1)/(1 - e^{-D/\beta\gamma c\tau})$ where d and D are the lengths of the beamline sections upstream and downstream of the tagger, β and γ the reduced velocity and Lorentz boost of the $\pi^\pm$, c the speed of light and τ the $\pi^\pm$ mean lifetime.

Table 1 Target configurations studied in the framework of the present study

Identifier	Length [cm]	Radius [mm]	Comment
A	70	5	Length of ENUBET proposed target [64]
B	70	13	Length of ENUBET proposed target [64] with T2K's target radius [63]
C	126.1	2.5	Length and radius of CNGS target [60]
D	126.1	13	Length of CNGS target [60] with T2K's target radius [63]
E	94	3.7	Length and radius of NuMI first design target [62]
F	91.4	13	T2K-like target [63]

hand, the high proton momentum a-priori favours the meson production at the momenta of interest ($p < 20\,\text{GeV}/c$), as phenomenologically demonstrated (e.g. the interested reader can observe the production maxima in [26] and [53], where the maximum production for secondaries of momentum p seems to lie within a fraction of 10–20% of the primary proton momentum). The authors decided to use a beam of an existing accelerator namely that of the CERN Super Proton Synchrotron (SPS) with a momentum of $p = 400\,\text{GeV}/c$. The assumption of the slow-extracted beam also defines essentially the focusing mechanism downstream of the target. In the case discussed here, the authors have employed large-aperture quadrupole magnets. Despite some potential increase in terms of beamline acceptance, magnetic horns have not been considered in this study given the complexity of production and optimisation [37]. Furthermore, these devices cannot easily be used in a slow extraction scheme since they cannot withstand heating beyond a few milliseconds. The magnets employed in the proposed design are existing magnets that have been used or are currently in use at CERN experimental areas [54], with known dimensions, properties, and characterised magnetic field gradients. The first-order optics was developed using TRANSPORT [55] and MADX [56], while the calculation of the hadronic interaction with the target material was performed using the well-known Monte Carlo software FLUKA [57,58]. Finally, a custom software package was developed to estimate the neutrino flux at the far detector based on the meson flux simulated with FLUKA.

3.1.1 Target and acceptance stage front-end

The high-intensity, high-momentum beam will be slow-extracted on a target to produce the mesons that will then generate the neutrino beam. The dominant production mode being $\pi^\pm \rightarrow \mu^\pm \overleftrightarrow{\nu}_\mu$ we limited our study to this mode. For this study, a dedicated optimisation effort has taken place in order to identify the best target for the described physics case. Various target geometries have been studied; literature research for various other neutrino beams (proposals and existing ones), like CERN Neutrinos to Gran Sasso (CNGS [59,60]), Neutrinos at the Main Injector (NuMI

[61,62]), Tokai to Kamioka (T2K [63]) and Enhanced NeUtrino BEams from kaon Tagging (ENUBET [64]), have demonstrated that graphite is the preferred material, due to its (relatively) low radiological impact and its robustness to high beam powers and temperatures. In our optimisation process, we started from lengths and radii values used or proposed in other facilities, combining the two to explore the relative effect of each parameter on the target properties. The different target configurations that demonstrated the best performance in our optimisation study, are summarised in Table 1. In our study, all the targets have been simulated in FLUKA as continuous rods of graphite (density 1.7 g/cm^3). Considering a right handed Cartesian coordinate system with the beamline aligned along the z axis, the 4-vectors of produced particles in terms of x, x', y, y', and total momentum p have been scored for all different targets in a perpendicular plane at $z = 0$ m, the starting point of the beamline, coinciding with the end surface of each target. The primary beam momentum was assumed to be in all cases $p = 400\,\text{GeV}/c$ for reasons discussed in the previous subsection.

As discussed in Sect. 1, different baselines covering different neutrino $E_1^{\text{vac.}}$ between 2.4 GeV and 6.0 GeV could in principle be envisaged, corresponding roughly to a pion momentum range of 6-12 GeV/c. The following target studies have been optimised for a reference pion momentum of 12 GeV/c (corresponding to a baseline of $\sim$ 2600 km with $E_1^{\text{vac.}}$=5.0 GeV), however, other momenta have also been taken into account as shown later on.

Figures 3 and 4 show a comparison, among the various targets, of the x (y) and x' (y') distributions for $\pi^\pm$'s at $z = 0$. In these plots, x (y) and x' (y') distributions are shown both for $\pi^\pm$'s covering the full momentum spectrum and for $\pi^\pm$'s having a reference central momentum of 12 GeV/c, considering a momentum spread of $\pm 25\%$. The dip observed in the $\pi^\pm$'s yield in the bottom right plot of Fig. 4, present in the longer and thinner targets identified as C and E in Table 1, is due to re-absorption of the forward emitted $\pi^\pm$'s ($x' < \arctan(R/L)$ where R is the radius and L the target length) by the target material. This is a combined effect of the target radius and length, as shown in Fig. 5. This figure represents the $\pi^\pm$'s angular divergence
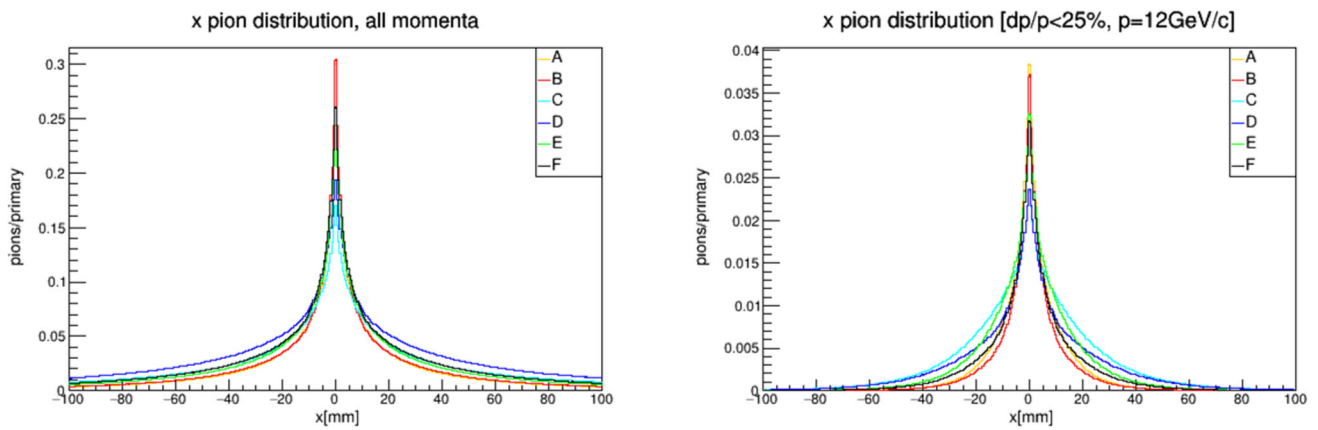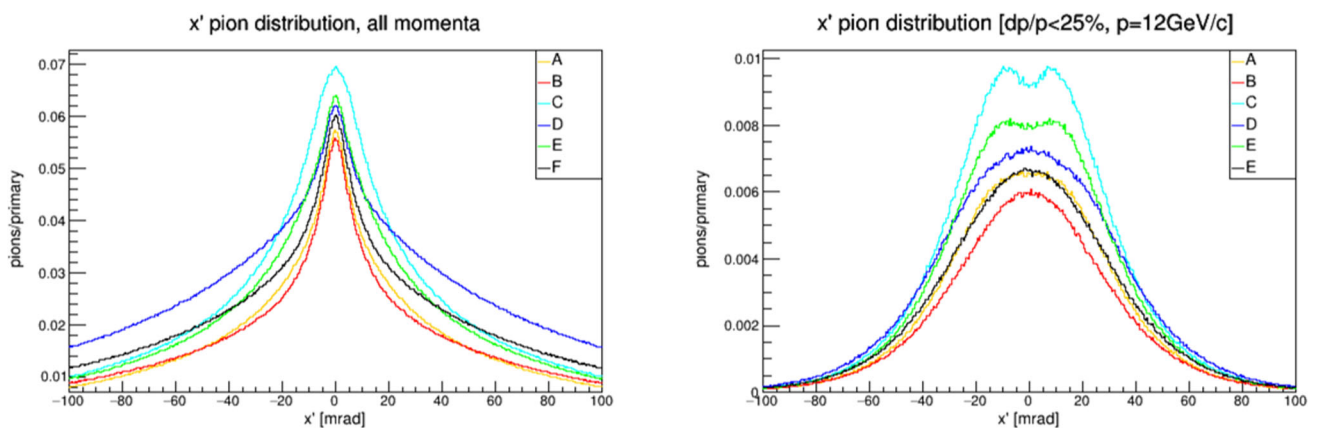
Fig. 3 x (y) distribution for $\pi^{\pm}$'s at $z = 0$. On the left, $\pi^{\pm}$'s covering the full momentum range; on the right, $\pi^{\pm}$'s having a reference central momentum of $12 \, \text{GeV}/c$ assuming a momentum spread of $\pm 25\%$

Fig. 4 x' (y') distribution for $\pi^{\pm}$'s at $z = 0$. On the left, $\pi^{\pm}$'s covering the full momentum range; on the right, $\pi^{\pm}$'s having a reference central momentum of $12 \, \text{GeV}/c$ assuming a momentum spread of $\pm 25\%$

x' as a function of the target depth for the targets C (Fig. 5a) and D (Fig. 5b), which share the same length but different radius. From the colour scale in Fig. 5a it emerges that the $\pi^{\pm}$'s in the considered momentum range are largely produced at angles $\arctan(R/L) \approx 2 \, \text{mrad} < x' < 20 \, \text{mrad}$ at the very beginning of target C, and therefore escape transversely through its sides without being reabsorbed, compared to $\pi^{\pm}$'s emitted in the forward direction, causing the dip in the distribution on the right of Fig. 4. Being an effect of the radius-to-length ratio of the target, the dip in the x' distribution disappears as the target radius gets larger and/or the target length smaller. Indeed, as shown in Fig. 5b, the larger radius of target D (13 mm) would require much larger emission angles $x' > \arctan(R/L) \approx 10 \, \text{mrad}$ for a $\pi^{\pm}$ to escape transversely through the target sides.[4] Since the probability of emission reduces very quickly for larger angles, the effective length seen by the $\pi^{\pm}$'s produced at the beginning

of the target is constant and the x' distribution at $z = 0$ is (approximately) Gaussian.

Taking into account the results of the aforementioned studies, target C has been chosen as our baseline. Further target optimisation could be envisaged, for example by considering spacing the target in different sections with gaps in between to reduce re-absorption, as done for the CNGS [60] and NuMI [61] targets. Besides our reference $p = 12 \, \text{GeV}/c \, \pi^{\pm}$ beam, in our study we also considered $\pi^{\pm}$ beams of $8 \, \text{GeV}/c$ and $6 \, \text{GeV}/c$. Figure 6 shows the position and angular distribution of $\pi^{\pm}$'s emerging from the target for different central momenta, considering a broad momentum spread of 25%.

In Fig. 6, the overall $\pi^{\pm}$ yield decreases as the central momentum decreases, with a significantly larger amount of $\pi^{\pm}$'s emitted at larger angles for the lowest momentum considered. In all cases, the peaks of the distributions are included in the $[-20, 20]$ mrad angular range. Therefore, a critical aspect of the beamline design is the optimisation of the angular acceptance, which needs to be maximised.

---

[4] The authors interpret x' as a measure of transverse (horizontal) angle. The rigorous expression is $x' < R/L$ if one decides to follow the definition of common accelerator-physics codes like MADX [56].

Fig. 5 Angular distribution of $\pi^{\pm}$'s in the $\pm 25\%$ momentum range around $12\,\text{GeV}/c$ emerging from the target C (**a**) and D (**b**), which share the same length but different radius, as a function of the target depth. The primary proton beam is impinging on the target front face from the left
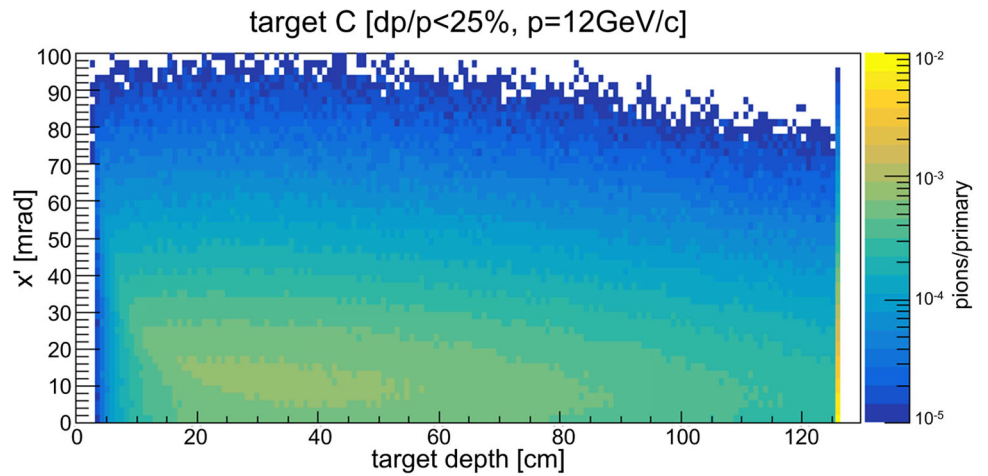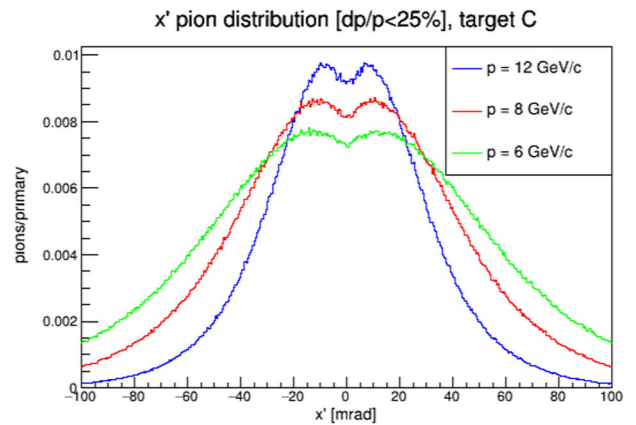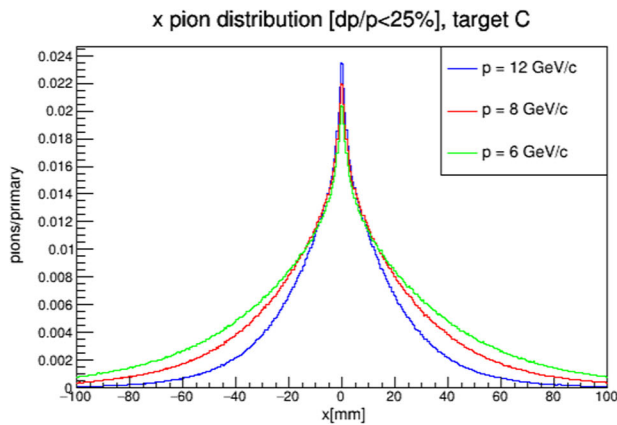

(a) Target C
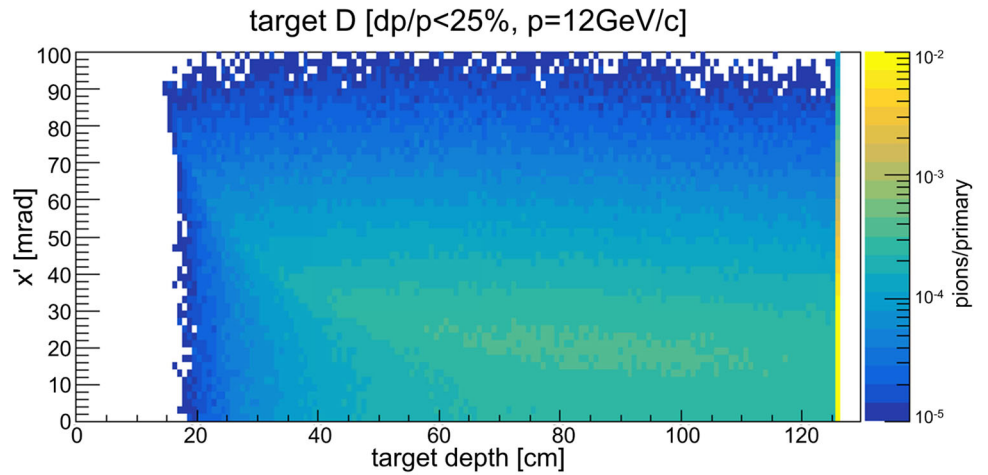
(b) Target D

Fig. 6 x (y) distribution (right) and x' (y') distribution (left) at $z = 0$ of $\pi^{\pm}$'s in the $\pm 25\%$ momentum range around different central momenta. The overall $\pi^{\pm}$ yield decreases with the central momentum, while a significantly larger amount of $\pi^{\pm}$'s is emitted at larger angles
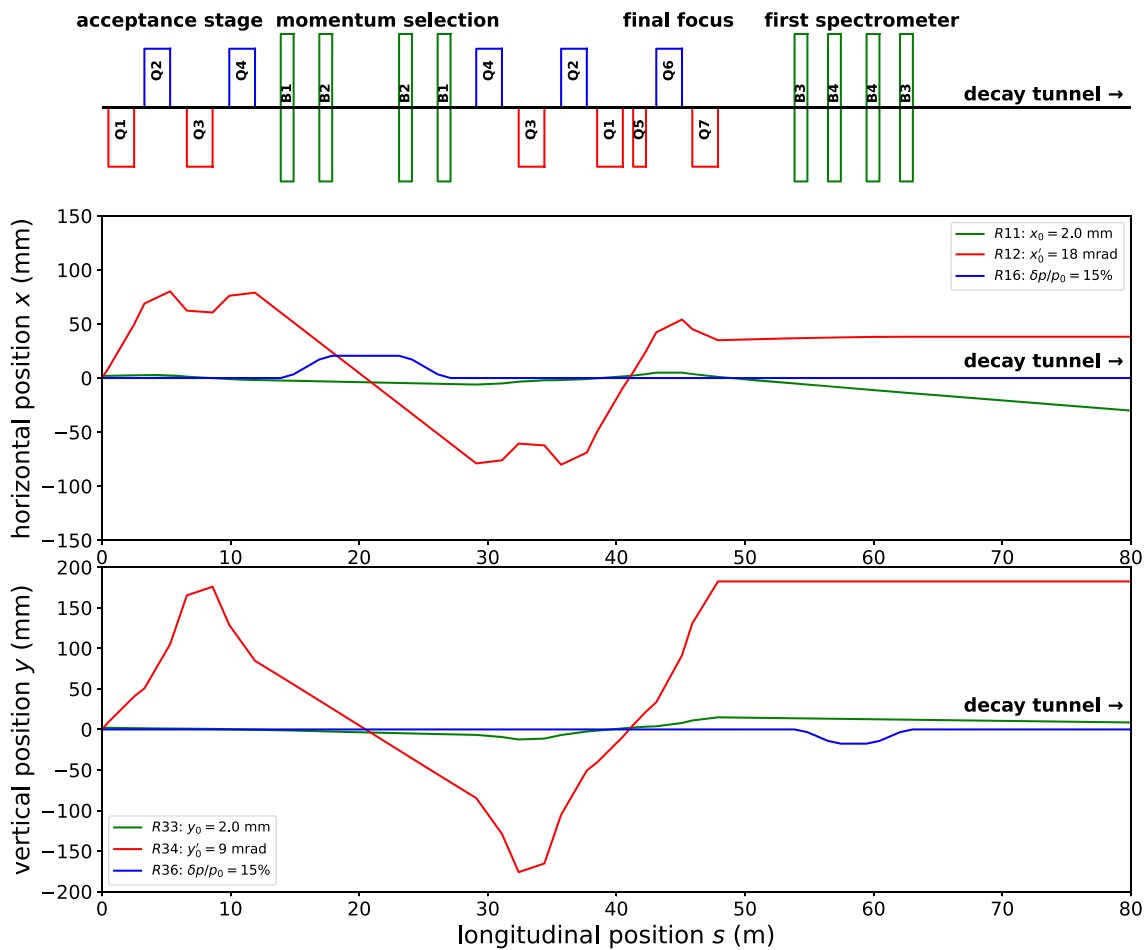
Fig. 7 First-order optics of the NuTag proposed beamline. The top sketch indicates whether quadrupoles are focusing (red) or de-focusing (blue) while the green boxes indicate bending magnets. Only the first 80 m of the beamline are shown. The second spectrometer is not shown in this plot to ease visualisation. Below the sketch, the two plots depict the horizontal (top) and the vertical (bottom) planes, respectively. The red lines correspond to the sine-like rays (particle has an initial trans-verse angle), the green lines to the cosine-like rays (particle has an initial transverse coordinate offset), while the blue lines to the dispersive ray [52] (particle has a momentum offset, indicated in the legend as a percentage of the central momentum). The tracking detectors are installed in the second achromat, just before the decay region as discussed in the text

3.1.2 First-order optics, momentum-selection and accepted phase-space

The first-order, transverse optics drawing of the proposed beamline is shown in Fig. 7. Downstream of the target, four quadrupoles (notated as *Q1*, *Q2*, *Q3* and *Q4*) ensure the acceptance of a large part of the phase space of particles produced at the target. This quadruplet, after an 180° phase-advance, brings the beam in both the bending and non bending planes and in both polarities, to a double focus in the middle of a first 4-bend achromat structure (*B1* and *B2*). The same names correspond to magnets that can be powered in series by the same power supply. The quadruplet, apart from allowing a large acceptance in both planes, preserves an absolute symmetry between the R-terms (transport matrix elements,

also called **R** matrix) of the horizontal and vertical plane up to the middle of the first achromat. At this exact position, the momentum selection takes place, with the π^+ and the π^- passing through two collimating holes of 10.25 cm radius placed respectively at $+18.25$ cm and -18.25 cm from the centre of a shielding block (see Fig. 8), which also acts as a primary beam dump as mentioned in Sect. 3.

Downstream of this initial momentum selection, a second quadruplet in series with the first, brings the momentum-selected beam to a 360° phase advance just before the final focusing stage. At this position, the beam can be cleaned with the use of collimators from background particles that have interacted with the magnets' apertures. At this stage, a quadrupole triplet (*Q5*, *Q6* and *Q7*) transports with a 90° phase advance the double polarity beam towards a second
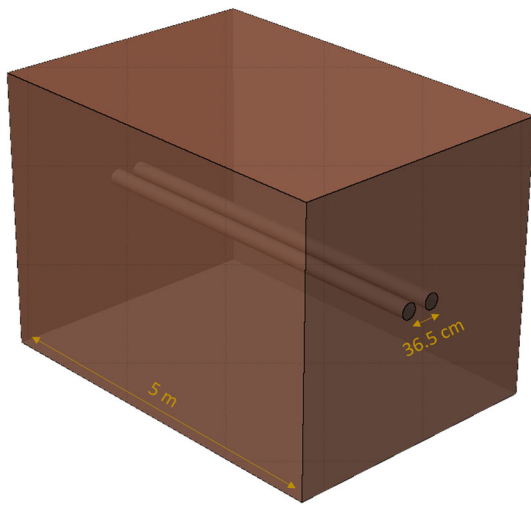
Fig. 8 Simplified model (visualised with FLAIR [65]) of the custom collimator structure placed in the middle of the first achromat, acting both as a momentum slit for the π^+ and π^- beams and as a primary beam dump. It consists of a 5 m long copper block, with two parallel holes to allow for the passage of the $\pi^{\pm}$ beams. These holes have a radius of 10.25 cm and a centre to centre distance of 36.5 cm

achromat (*B3* and *B4*), similar to the first but vertically oriented. The reason for the inverse orientation compared to the upstream achromat was a slight reduction in the acceptance caused by the large spot size of the beam in the horizontal plane. Also, a vertical orientation favours the placement of shielding in both sides of the tunnel in case this was needed for background reduction. Tracking stations are installed around and inside the second achromat in order to measure the momentum, direction, position and time of all the charged particles, on an event-by-event basis. The large R11 and R33 matrix elements in the horizontal plane along with the 900 m length of the decay tunnel will inevitably result in a transverse beam size of the order of $\mathcal{O}$(m) at the final tracking station, taking also into account the muon decay angles. For this reason, large aperture dipoles such as GOLIATH [66] or MORPURGO [67], present today in the North Area at CERN, can serve as spectrometers in the second (downstream) tracking station, the details of which lie beyond the scope of this paper.

The described optics predict an angular acceptance of $\mathcal{O}$(20)mrad in the horizontal and $\mathcal{O}$(9)mrad in the vertical plane, as will be discussed later in Sect. 4.

As already mentioned, the part of the primary beam that does not interact with the target ($<< 1\%$), is dumped on the large collimator structure (shown in Fig. 8) located between the two bending dipoles of the first achromat. Indeed, a sufficient separation between the π^+ and π^- beams (roughly 27 cm distance between the two polarities for the central momentum, the primary proton beam axis laying in the middle) ensures that the $\pi^{\pm}$ beams pass through the holes and continue downstream, while the protons and all the neutral

or off-momentum charged particles are stopped. The collimator/dump structure proposed here is purely conceptual, serving as a first assumption, and a proper engineering design would have to follow in future studies.

3.2 Meson tracking station

The beam spectrometer has the purpose of measuring the time, position, direction, charge and momentum of all charged beam particles. The detector design is conceptually similar to that of the NA62 GigaTraKer (GTK) [20,68] and its proposed upgrade for the High Intensity Kaon experiments (HIKE) [69]. The spectrometer is placed at the second achromat and is composed of a set of tracking stations made from silicon pixel detectors which are located before, after and inside this achromat. The station should be as thin as possible to reduce the multiple Coulomb scattering of particles. A material budget of 0.5% X_0 per station was achieved for the NA62 GTK.

The measurements from all the stations allow the trajectory and momentum of each beam charged particle traversing the achromat to be reconstructed. Indeed, apart from scattering effects, the trajectories of the particles before and after the achromat are aligned and parallel to the trajectory described by the particle in the innermost drift space of the achromat. The distance between these parallel trajectories is inversely proportional to the particle momentum. As for the NA62 GTK [20], the material budget of the station is expected to be one of the dominant factors limiting the precision to which the particle's direction and momentum can be determined.

For a configuration with three tracking planes, placed before, after and inside the achromat, as the initial GTK design, the momentum resolution can be expressed as [70]:

$$\frac{\delta p}{p} = \frac{1}{\Delta} \cdot \sqrt{\sigma_y^2 + A^2 + B^2 + C^2}, \qquad (2)$$

with

$$A = \frac{\sigma_y \cdot d_{12}}{d_{12} + d_{23}}$$
$$B = \frac{\sigma_y \cdot d_{23}}{d_{12} + d_{23}}$$
$$C = \frac{\delta_{\mathrm{MCS}} \cdot d_{13} \cdot d_{23}}{d_{12} + d_{23}},$$

where

- Δ is the distance between the trajectories inside and outside the achromat for the nominal momentum and is determined by the dipole magnet bending angle,
- d_{12}, d_{13} and d_{23} are the distances along the z-axis between the first and second, the first and third and second and third tracking planes,
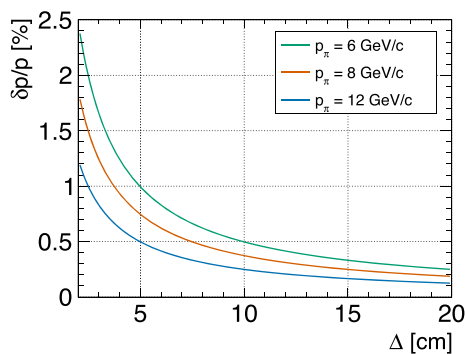
Fig. 9 Momentum resolution of the π^+ beam, provided by the meson spectrometer, assuming 6 m spacing between consecutive tracking stations, a pixel size of 45 μm and a tracking plane thickness equivalent to 0.5% X_0

- σ_y is the resolution on the y coordinate of the particle at the tracking planes and is proportional to the pixel size,
- δ_{MCS} is the mean scattering angle due to the multiple Coulomb scattering in the tracking plane.

The momentum resolution is shown as a function of Δ in Fig. 9, assuming 6 m spacing between consecutive tracking stations, a pixel size of 45 μm and a tracking plane thickness equivalent to 0.5% X_0. In the proposed beamline, $\Delta = 11.7$ cm for a bending angle of 45 mrad, which corresponds to a $\delta p/p$ of 0.21% for a 12 GeV/c pion beam. The $\pi^{\pm}$ momentum resolution provides a good estimate of the neutrino energy resolution for a LBL setup, as the energy of a neutrino emitted collinear to the $\pi^{\pm}$ is $0.43 \cdot E_{\pi}$, where E_{π} is the $\pi^{\pm}$ energy. Hence, as long as Δ is larger than 5 cm, a tagged neutrino experiment is able to provide a neutrino energy resolution better than 1%.

The pixel technology considered for the station is similar to the one envisaged for the high luminosity phase of the LHC experiments [71] and is expected to be able to operate at a particle flux as high as $10 - 100$ MHz/mm^2 [21] and at an integrated fluence of up to 10^{16-17} n$_{\mathrm{eq}}$/cm^2. The former specification sets a strong constraint on the peak flux of charged beam particles at the second achromat. In addition, the beam transverse size should remain smaller than 0.1 m^2 since assembling larger pixel modules with a material budget of 0.5 % X_0, i.e., about 500 μm of silicon, would be mechanically challenging to produce.

4 Simulated performance

In order to validate the operational principle of the beamline, a full FLUKA model has been developed up to the second achromat. Its geometrical layout is shown in Fig. 10. This model includes a complete description of the two-dimensional magnetic field map (both in the gap and in the

yoke) for each quadrupole present in the beamline, since the magnets used for this study (QPL and QPS [54]) are well characterised and currently in use in many secondary beamlines at CERN. For the bending magnets, however, an uniform field throughout the aperture and zero field in the yoke is assumed. To transport simultaneously π^+ and π^- beams with large angular acceptance and to ensure a satisfactory momentum selection, bending magnets with larger horizontal apertures than the ones currently present at CERN would be necessary. These magnets, would be identical to the existing MBPS magnets in use today (and described also in [54]) just with a larger horizontal aperture of 600 mm. The characteristics of the proposed magnets are summarised in Table 2.

In our study, we employed a simple and robust methodology in order to (a) precisely calculate the neutrinos expected in the far detector while (b) avoiding performing computationally expensive Monte Carlo simulations and/or variance reduction techniques that could create extra uncertainties in the final yield. Specifically, we followed the steps listed below:

1. Following the target optimisation described in Sect. 3.1.1, we subsequently validated the hadron beam optics and the resulting acceptance based on analytic calculations. At this stage, we made sure that no elements are overly restricting the acceptance and we confirmed the robustness of our computational framework (see Sect. 4.1).
2. Subsequently, using the developed FLUKA model for the beamline and based on the analysis in Sect. 4.1, we calculated the expected transmission through the beamline (see Sect. 4.2). We validated the overall beamline behaviour by running a fully detailed simulation of the beamline, including the primary beam interaction with the target as well as all the magnetic elements and collimating structures down to the beginning of the decay region.
3. Using the results from the step above, we performed analytic kinematic calculations for the expected number and momenta of neutrinos that will reach the far detector (see Sect. 4.4).

In the sections below, we describe the steps in detail.

4.1 Linear acceptance calculation

As a first step, we evaluated the phase space of accepted $\pi^{\pm}$'s that can be transported from the target to the end of the beamline. This acceptance depends strongly on the aperture limitations of the line, defined by the magnets' apertures, the collimator holes and the beam pipes. The beam size and angular distribution in each element of the line is defined (in first-order) by the transport matrix, that can be easily retrieved via any optics code or even by analytical calculations. By projecting the individual apertures backwards and
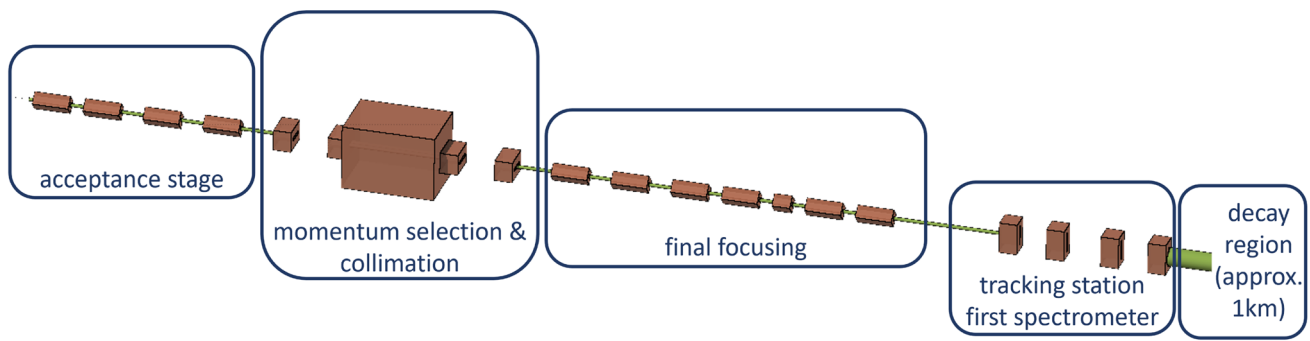
Fig. 10 FLUKA model of the proposed beamline, visualised with FLAIR. The acceptance stage is followed by the collimation and momentum selection station, while afterwards the beam is transported to the downstream tracking station and first spectrometer. The modelling of the second meson tracking station and dump shown in Fig. 2 is beyond the scope of this study

Table 2 Specifications and characteristics of the magnet types used in this study [54]. A possible adaptation of the MBPS bending magnet, with a larger aperture width (600 mm compared to the standard 300 mm), has been considered in the FLUKA simulations, to allow for the simultaneous transportation of both pion polarities

Name	Type	Length [m]	Aperture type	Aperture radius [mm]	Aperture width [mm]	Aperture height [mm]	Peak field (Gradient) [T] ([T/m])
QPS	Quadrupole	1	Circular	100	–	–	10.5
QPL	Quadrupole	2	Circular	100	–	–	10.5
MPBS	Dipole	1	Rectan.	–	300/600	140	1.84

mapping the apertures to the beginning of the line, it is possible to identify the limiting apertures and thus the fraction of pions emitted from the target that would eventually be transported to the end of the line.

Figure 11a and b show the accepted phase space for the nominal momentum in the horizontal and vertical planes for π^+ and π^- respectively. As anticipated from the first-order optics calculation shown in Fig. 7, the maximum horizontal and vertical angular acceptances are ~ 20 mrad and ~ 9 mrad for π^+ and inverted for π^-. On the other hand, the horizontal and vertical position acceptances are ~ 15 mm and ~ 25 mm for π^+ and the opposite for π^-. The differences observed in the $\pi^\pm$ accepted phase spaces, already at the first order optics level, are due to the asymmetric aperture of the bending magnets that constitute the two achromats. Indeed, the small vertical gap (140 mm) of the MBPS magnets constrains strongly the y' acceptance for the π^- beam, while the acceptance of the π^+ is constrained by the majority of elements present in the line, in both planes.

Particles with momenta different from the nominal momentum however, are subject to chromatic aberrations that become particularly important for large momentum offsets. For momentum offsets beyond $|\delta p/p_0| > 10\%$, the limit of the applicability of linear optics is reached, since the first-order approximation (used in the TWISS module of MAD-X used to calculate the optics) is no longer valid [72]. For a more accurate evaluation of these particles' trajecto-

ries, a Monte Carlo simulation was used as will be shown in Sect. 4.2.

4.2 FLUKA simulations and beamline transmission calculation

The acceptance selection criteria calculated in the previous step, and depicted by the red lines in Fig. 11a and b have been applied to the $\pi^\pm$ yields produced by the target simulations and scored in FLUKA, as described in Sect. 3.1.1. The results of this selection are shown in Fig. 12 for $\pi^\pm$ in a $\pm 1\%$ momentum range around 12 GeV/c, to stay within the validity limits of the first order optics and avoid second order chromatic effects.

Starting from the identified accepted phase space, and assuming a 1% momentum acceptance, we performed extensive FLUKA simulations to validate the transmission of the momentum-selected hadron beams through the beamline (i.e., excluding all background), modelling all elements outside the beam pipe as "blackhole" i.e., a fully absorbent material that prevents any further transportation of interacting particles. The result of these simulations is shown in Fig. 13. It can be seen that for this small momentum spread, the beam trajectory is in very good agreement with the linear optics for both π^+ and π^-. At the momentum-selection position, the slight astigmatism observed between the horizontal and vertical plane, is due to the slightly different magnifi-
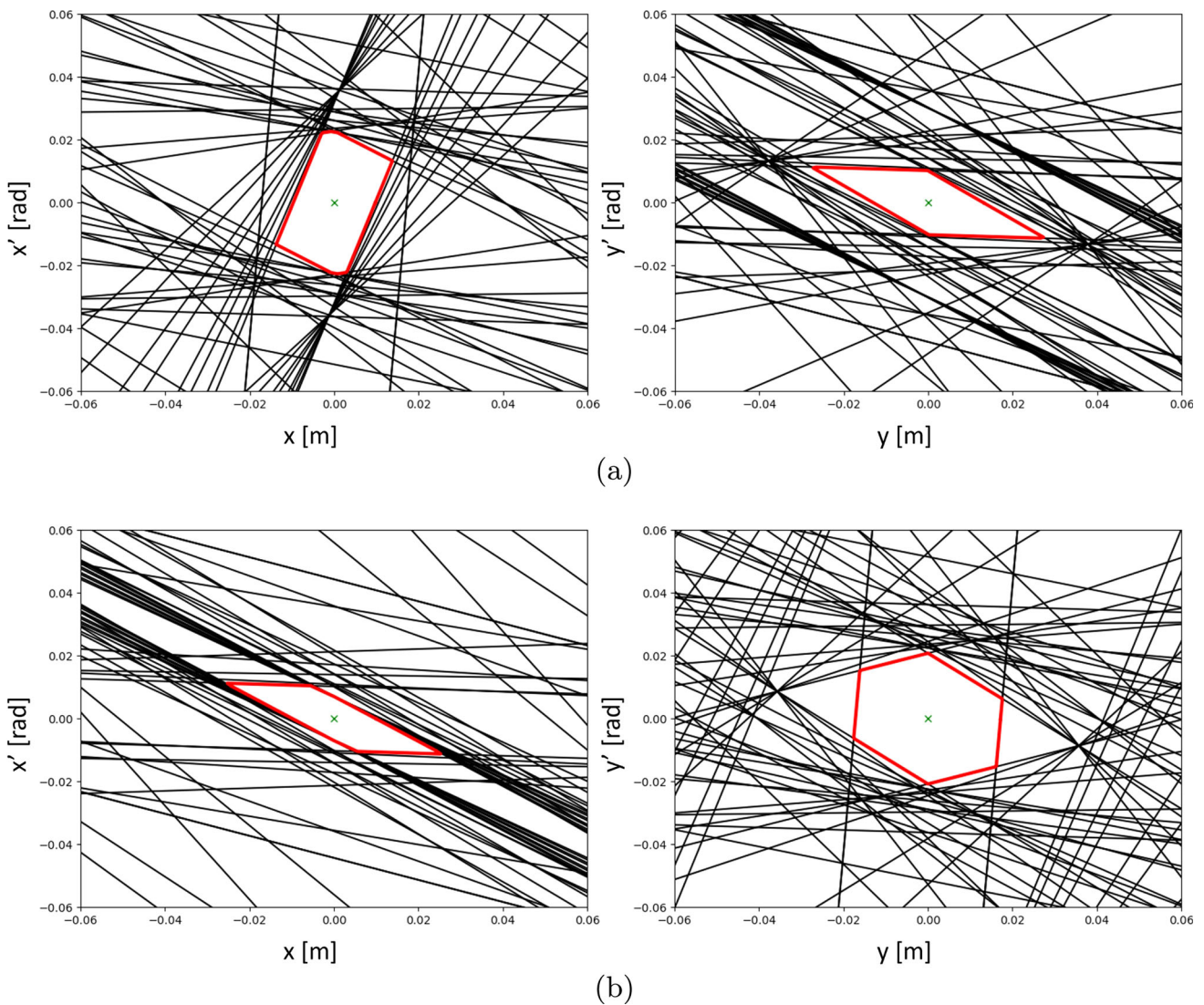
(a)

(b)

Fig. 11 Accepted phase space of the nominal momentum π^+ (**a**) and π^- (**b**) beam: (left) horizontal plane and (right) vertical plane. Each of the black lines corresponds to an aperture limitation along the beamline at some point s projected backwards to the start of the line. The red polygon represents the remaining accepted phase space, obtained by connecting the intersection points of the innermost aperture limitations. Compared to π^+, the π^- y' acceptance is strongly constrained by the vertical gap of the first and last bending magnets in the first achromat

cation terms (green dashed lines in Fig. 7) along with the dispersion present in the horizontal plane. The result is that the beam waist is displaced by a few cm upstream.

4.3 Detailed simulation of the beamline and calculation of momentum acceptance

To obtain a fully realistic estimation of the number of the $\pi^\pm$ transmitted through the line and their momentum distribution (that defines the momentum acceptance of the beamline), a second simulation was performed using the whole target sample as a source. From this simulation, we derived the momentum distribution of the transmitted pion beams that

we show in Fig. 14 for three different reference momenta. It can be seen that the centroid of the π^+ and π^- distributions do not coincide exactly, with the former having a peak at around $p = 12\,\mathrm{GeV}/c$ while the latter displaying its peak at $p = 13\,\mathrm{GeV}/c$ for a $p = 12\,\mathrm{GeV}/c$ reference momentum. This effect can be explained by second order aberrations and is independent of the reference momentum chosen, since the two beams π^+ and the π^- have waists in different positions along z, compared to the focus position, and therefore are (slightly) differently momentum-selected.

The higher-momentum particles observed in Fig. 14 especially in the π^+ beam are a consequence of the wider horizontal phase space and the particular configuration chosen
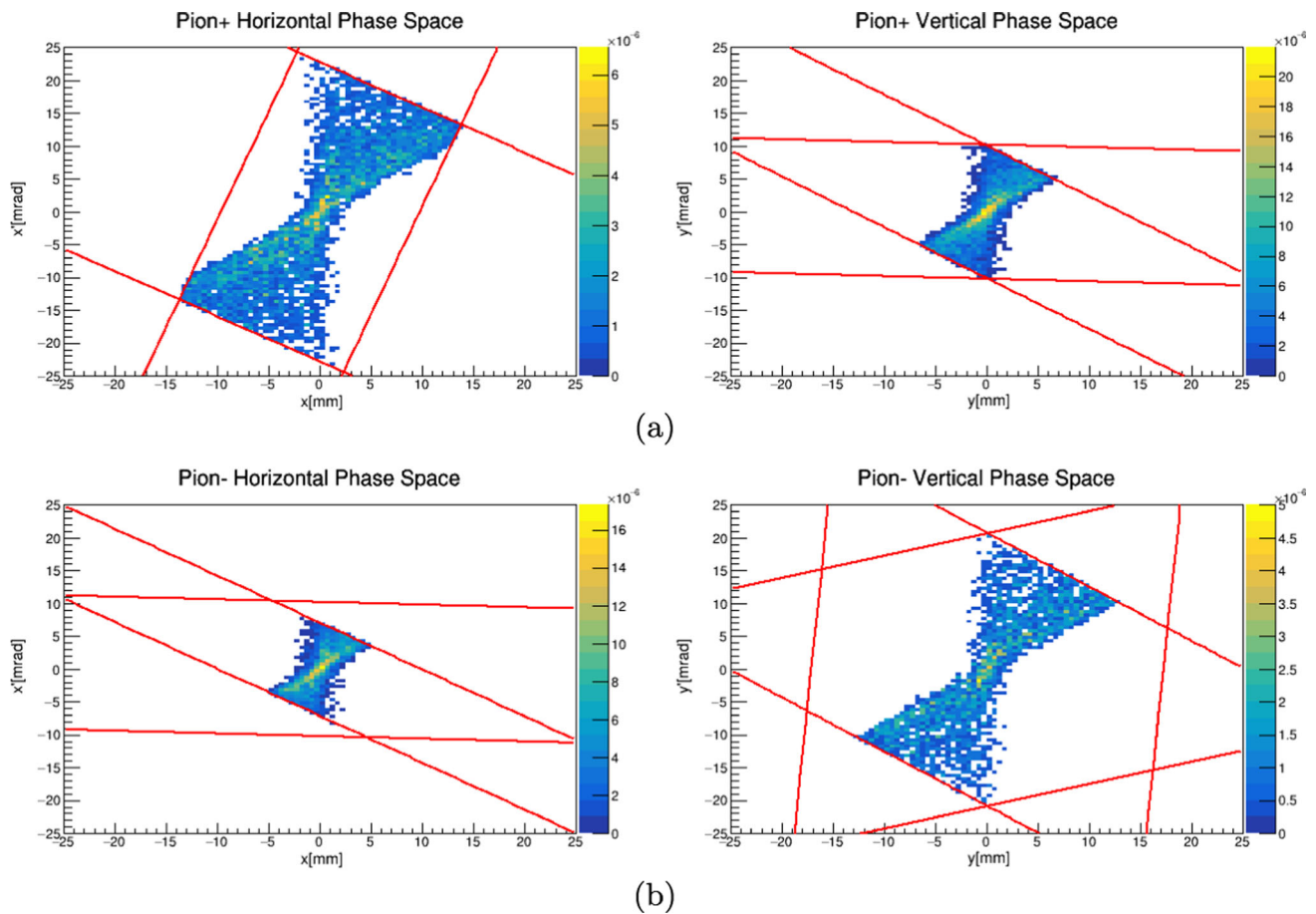
Fig. 12 Target sample π^+ (**a**) and π^- (**b**) accepted phase space in the $\pm1\%$ momentum range around $12\,\mathrm{GeV}/c$. The selection criteria identified in Sect. 4.1 have been applied to the $\pi^\pm$ yields emitted by the target, obtained from FLUKA simulations, to identify the phase space theoretically transported through the line. Results are normalised per primary proton. As expected by the linear optics, the horizontal plane of the π^- is very similar to the vertical plane of the π^+ and vice-versa, as discussed in the text

for the collimator apertures. This collimator is 5 m (≈ 30 interaction lengths) long to ensure the complete absorption of the primary proton beam as well as a satisfactory absorption of the secondaries produced by the primary beam interaction with it. For this reason, the collimating slits of the π^+ and π^- beams are effectively much larger than what strictly required by the $\mathcal{O}(25\%)$ theoretical momentum acceptance (10.25 cm radius compared to 3.43 cm radius). Indeed, while the beam has a waist around the slit position, the size of the accepted beam at its entrance and exit is larger (see Fig. 13) and therefore the momentum selection is less stringent. Furthermore, the wide horizontal angular acceptance for the π^+ beam in combination with the large aperture holes, allows for some π^+ mesons with higher momenta and large angles to be transported through the beamline, as shown in Fig. 15. The overall content of the high-momentum tail is about 20% of the total, and has been quantified by comparing the histogram integral in two different ranges: [0, 16] GeV/c and [16, 30] GeV/c.

The simulation also allows for the estimation of the beam transverse size and particle flux at the second achromat. As explained in Sect. 3.2, the limitations of the tracker technology require the beam size to be < 0.1 m^2 and the rate 10–100 MHz/mm^2. Figure 16 shows a two-dimensional map of the beam particle flux at the exit of the second achromat. The two specifications are fulfilled with a beam size of about 15×50 cm^2 and a peak flux of < 15 MHz/mm^2, considering an impinging primary proton beam of 2.5×10^{13} protons/spill with a spill length of 4.8 s.

4.4 Neutrino yield evaluation at the far detector

Knowing the total number as well as the full 6D phase space (x, x', y, y', dp/p, z) of the pions transmitted through the beamline it is possible to precisely calculate the expected neutrino yield at the far detector. To do so, a custom calculation code has been developed.
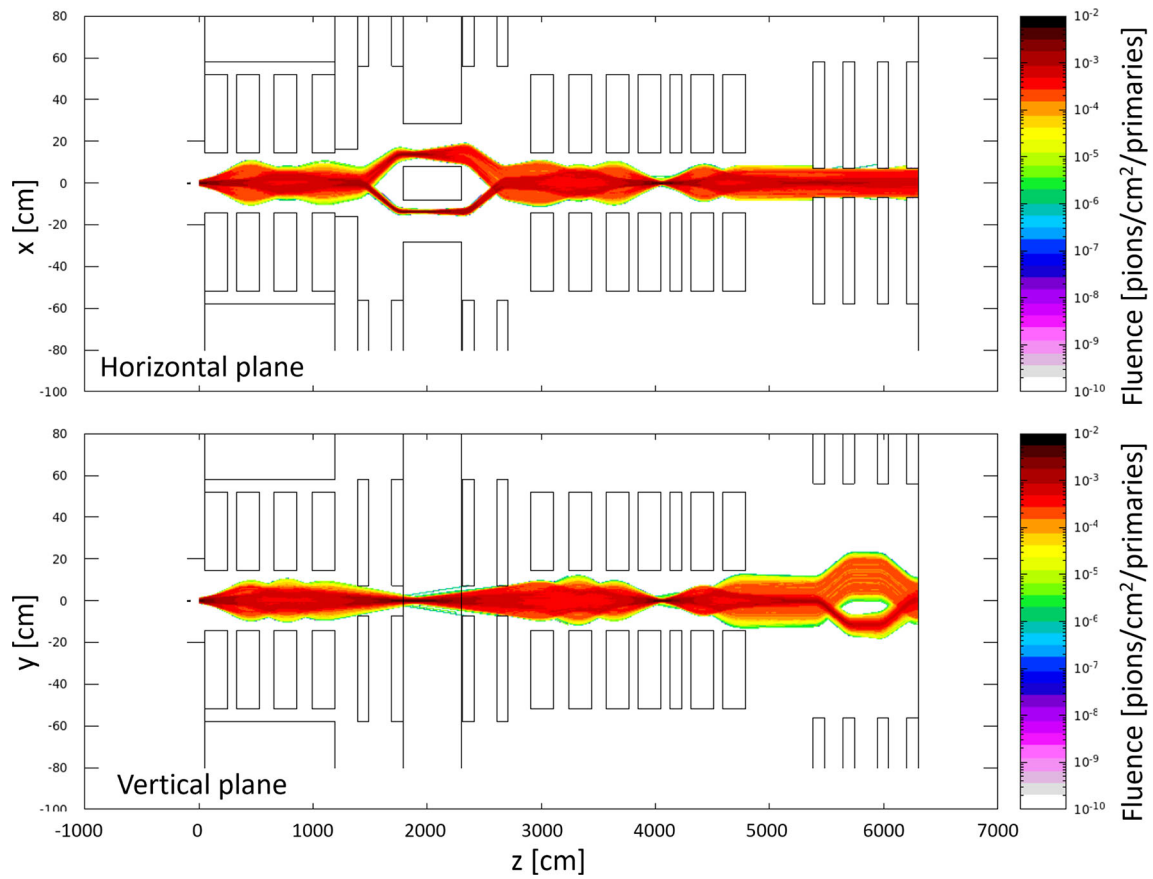
Fig. 13 FLUKA simulation of accepted π^+ and π^- phase spaces identified in Fig. 12 transported through the beamline. (Top) horizontal and (Bottom) vertical planes. All the results are normalised per primary proton. The trajectories of the particles inside the decay region are not shown

Fig. 14 Momentum spectrum of $\pi^\pm$'s at the start of the decay region, after having been transported through the beamline. The spectrum is shown for three different beamline momenta p: 12 GeV/c (solid line), 8 GeV/c (dashed line) and 6 GeV/c (dotted line). The individual contribution to the full spectrum (black) of π^+ (red) and π^- beams is also shown for each reference momentum
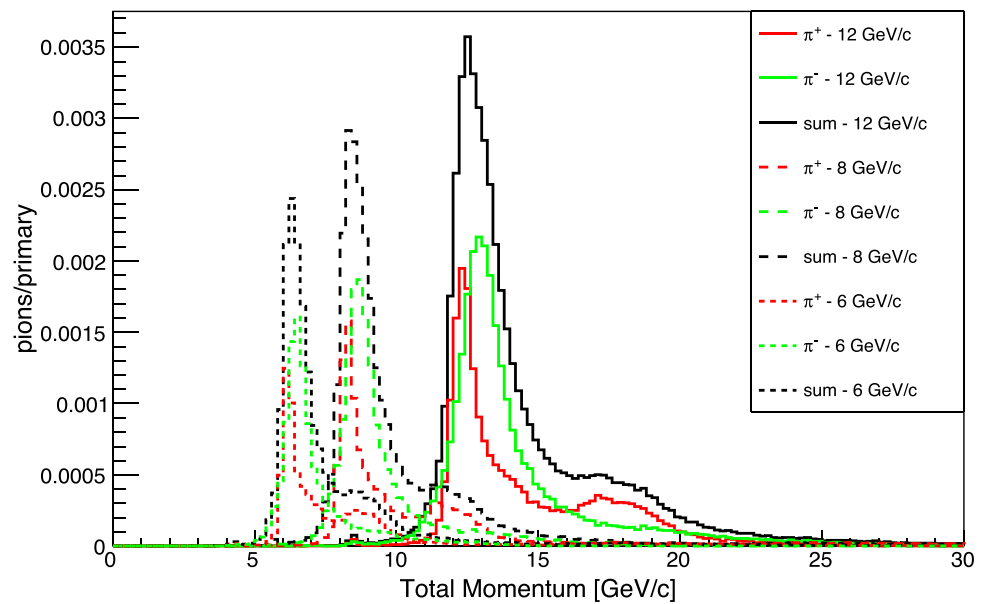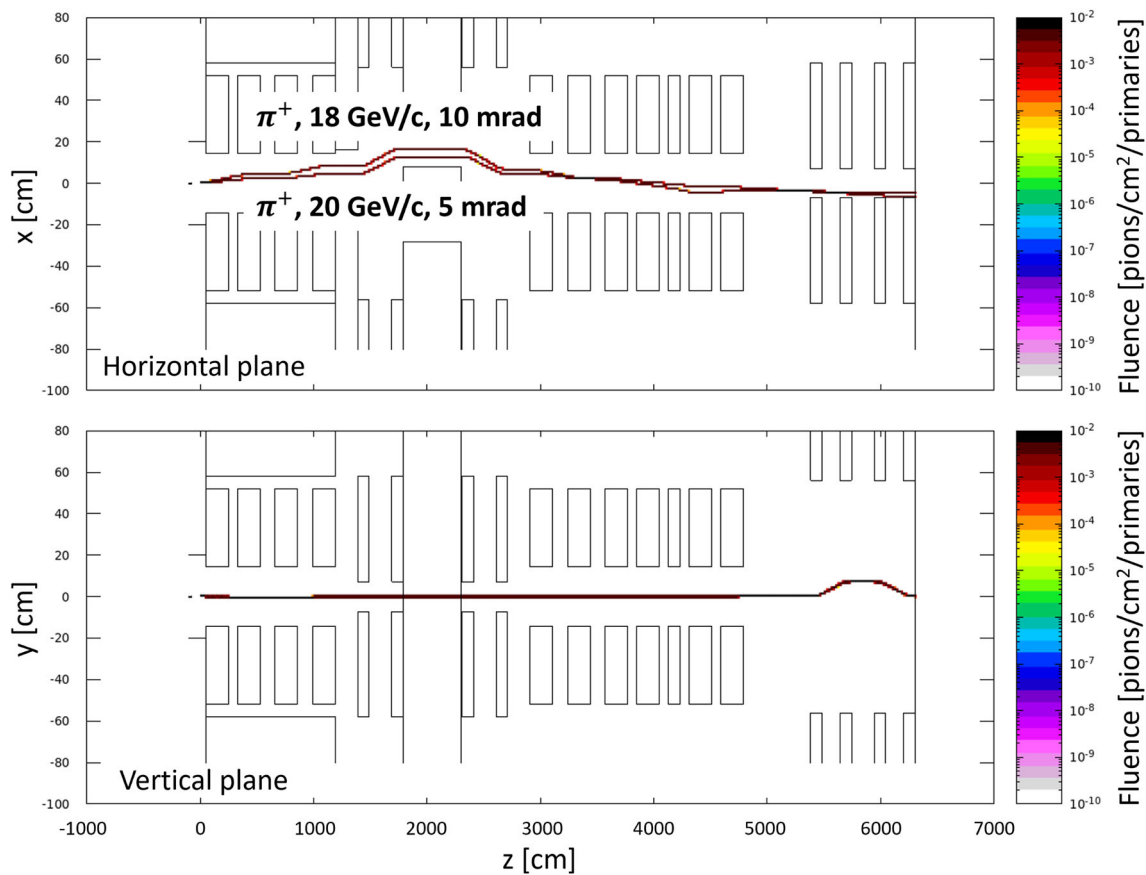
Fig. 15 Two example trajectories of higher momentum π^+'s, 18 GeV/c and 20 GeV/c, emitted at large angles from the target, 10 mrad and 5 mrad, respectively, and their transmission through the beamline. These larger momentum, but large offset particles constitute the species that populate the peaks averaged around 8 GeV/c, 11 GeV/c and 18 GeV/c that can be seen on the right of the central momenta peaks of 6 GeV/c, 8 GeV/c and 12 GeV/c in Fig. 14

The software, developed in C^{++}, generates $\pi^\pm$'s at the exit of the second achromat by sampling, for π^+ and π^- separately, the x, y two-dimensional distribution and p, x', y' three-dimensional distribution obtained from the FLUKA simulation at this position. For each $\pi^\pm$, the z coordinate of a decay vertex, z_{vtx}, is generated on an exponential distribution with a decay constant of $1/(\beta\gamma c\tau)$ where β and γ are the reduced velocity and Lorentz boost of the decaying $\pi^\pm$, c the speed of light and τ the $\pi^\pm$ mean lifetime [73]. Each $\pi^\pm$ is then propagated to this z_{vtx} where the $\pi^\pm \rightarrow \mu^\pm \overleftrightarrow{\nu}_\mu$ is generated using standard decay kinematics [74]. The resulting $\overleftrightarrow{\nu}_\mu$ are then propagated to the far detector, which is assumed to have a transverse half-size of 100 m. The neutrino energy distribution at the far detector is obtained from the distribution of the generated $\overleftrightarrow{\nu}_\mu$'s which occur in the far detector acceptance. The flux per Proton On Target (POT) is obtained by scaling the previous distribution by the ratio of $\pi^\pm$ per POT at the second achromat exit (obtained from FLUKA) and the number of generated $\pi^\pm$. The annual fluxes are shown in Fig. 17 assuming 1.8×10^{19} POT per year. This number cor-

responds to 2.5×10^{13} protons per spill, 3000 spills per day, 30 days per month over the course of 8 months in a year of operation. In such conditions, the radiation resistance of the silicon pixel detector (see Sect. 3.2) would allow the experiment to operate for about 10 years. The annual rates of signal neutrinos in the ν_e and $\bar{\nu}_e$ appearance channels and around the energy of the first oscillation maximum are reported in Table 3 for LBL experiments using the flux reported in Fig. 17 and a 10 Mton detector.

At the energy of the first oscillation maximum, the beamline is thus able to deliver a neutrino flux that would allow the collection of a neutrino sample with a size comparable to the ones of the upcoming LBL experiments with megaton-scale natural water Cherenkov detectors. While systematic uncertainties are expected to be a limiting factor for the latter, they should be better controlled for the former due to the tagging technique. Hence, a new generation of tagged LBL experiments, exploiting the beamline developed in this study, could be able to improve the knowledge on the neutrino oscillation in a sustainable way. Indeed, it requires beam pow-
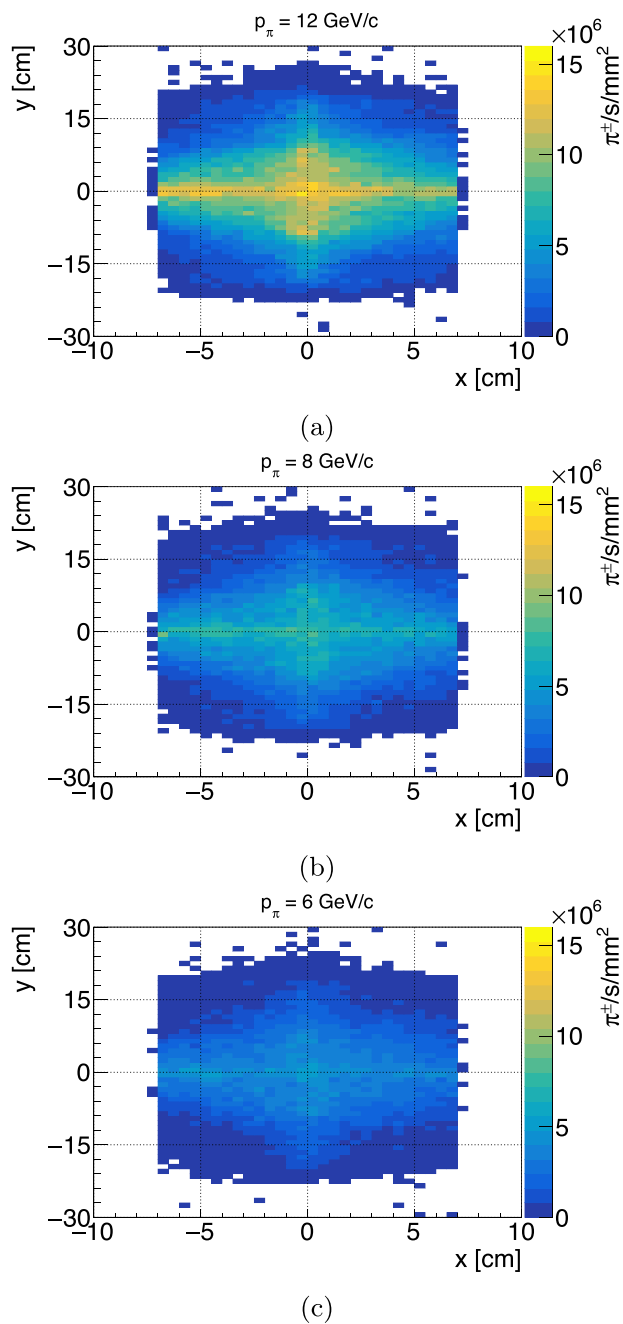
(a)

(b)

(c)

Fig. 16 (x, y) map of the $\pi^{\pm}$ flux after the second achromat ($z = 63$ m) obtained from the FLUKA simulation for a beamline with a nominal $\pi^{\pm}$ momentum of 12 GeV/c (**a**), 8 GeV/c (**b**) and 6 GeV/c (**c**), considering an impinging primary proton beam of 2.5×10^{13} protons/spill with a spill length of 4.8 s

(a)

(b)

Fig. 17 ν_{μ} (**a**) and $\bar{\nu}_{\mu}$ (**b**) fluxes from pion decays in the far detector acceptance for beamlines with nominal energies of 12 GeV (dark blue), 8 GeV (green) and 6 GeV (light blue) overlaid with the minimal neutrino fluxes required to collect as many detected neutrino as DUNE [10] at the first oscillation maximum for a 5 Mton (dashed black) and a 10 Mton (solid black) detectors

carried out to assess more quantitatively the physics potential of such experiments.

5 Summary and discussion

The work presented here aimed to introduce a novel beamline concept for long-baseline neutrino beam experiments, allowing the implementation of the neutrino tagging technique. This technique relies on the operation of charged particle spectrometers instrumented with trackers and installed in the beamline to kinematically reconstruct the $\overleftrightarrow{\nu}_{\mu}$ from $\pi^{\pm} \rightarrow \mu^{\pm} \overleftrightarrow{\nu}_{\mu}$ and $K^{\pm} \rightarrow \mu^{\pm} \overleftrightarrow{\nu}_{\mu}$ decays. The operation of these trackers limits the beam particle flux and size. Indeed, at the tracker location, the charged beam particle flux has to be 10–100 MHz/mm^2 and its transverse size has to be

ers of $(10 - 100)$ kW which, first, are much lower than the $\mathcal{O}(1)$MW beams of the upcoming experiments and of most of the proposed options for the next generation of LBL neutrino experiments [75,76] and, second, are partially available in existing facilities (however, not directly at the required intensity of 1.8×10^{19} POT per year). Dedicated studies should be
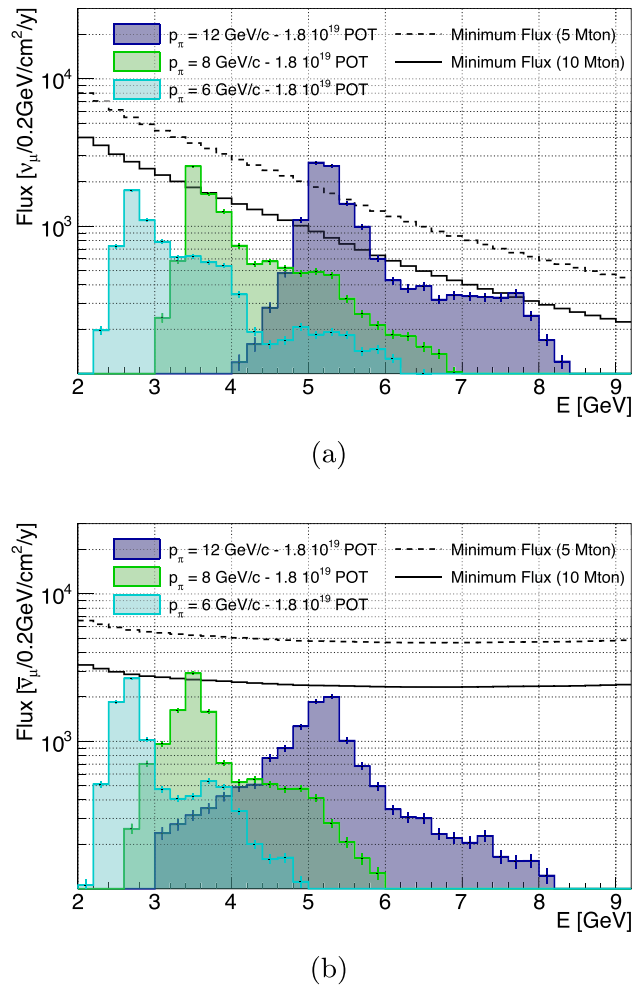
Table 3 Expected annual rates of signal neutrinos in the ν_e and $\bar\nu_e$ appearance channels in a ± 0.1 GeV window around the energy of the first oscillation maximum (E) for DUNE [10] and LBL experiments employing a 10 Mton detector with our beam line. The baseline of each experiment is chosen such that the first oscillation maximum energy matches the energy at the spectrum peak shown in Fig. 17

E [GeV]	Nb of ν_e [/0.2 GeV/y]	Nb of $\bar\nu_e$ [/0.2 GeV/y]	Comments
2.5	27.3	6.9	DUNE [10]
5.2	84.4	4.7	This study with $p_\pi = 12$ GeV/c
3.5	38.0	6.7	This study with $p_\pi = 8$ GeV/c
2.7	17.5	5.7	This study with $p_\pi = 6$ GeV/c

< 0.1 m^2, constraints which result in a lower neutrino flux, compared to standard LBL neutrino experiments. This low neutrino flux is compensated by the use of $\mathcal{O}(1)$ Mton natural water Cherenkov detectors which are two orders of magnitude larger than the ones used in standard LBL neutrino experiments but allow for much lower precision on the neutrino characteristics. In a tagged experiment, this lower precision is compensated by kinematic reconstruction that gives the neutrino energy with $< 1\%$ energy resolution and determines the neutrino's initial flavour and chirality.

The beamline studied in this work, allows the simultaneous transportation of π^+ and π^- beams, halving the required run time to collect neutrino and anti-neutrino data. In addition, for measurements such as the charge-parity violation phase, δ_{CP}, where the oscillation probabilities of neutrinos and anti-neutrino are compared, the ability to collect both chiralities simultaneously might reduce systematic uncertainties arising from differences in data-taking conditions between neutrino and antineutrino runs. To fulfill the constraints on the particle flux, the beamline was designed to operate with a slow-extracted proton beam. The study was performed assuming a 400 GeV/c proton beam and, for this momentum, a graphite target of ≈ 1.2 m was found to yield the largest amount of secondary $\pi^\pm$. In a tagged beamline the neutrino flux is limited by the sustainable charged particle flux at the spectrometer which must be < 100 MHz/mm^2. In the beamline proposed here, this flux is only 20 MHz/mm^2 per 2.5×10^{13} protons/spill over a spill of 4.8 s. Hence, a significant margin is available to further improve the $\pi^\pm$ yield.

With our study and the proposed tagged beamline, we demonstrated that it is possible to collect neutrino interaction samples with a size comparable to the one expected for upcoming experiments using beams of much lower power. Detailed physics analyses, beyond the scope of this study, should be performed to evaluate the physics potential of a tagged experiment employing the proposed beam line. However, as the tagging technique is expected to offer an improved control of several key systematic uncertainties limiting the sensitivity of these upcoming experiments, our tagged beamline offers a valuable option to further improve the knowl-

edge on the neutrino oscillation parameters. At such tagged experiments, the precision on these parameters would then be limited by the size of the neutrino samples and thus by the neutrino fluxes. Therefore, any effort in the direction of improving the beamline performance should aim to maximise the $\pi^\pm$ yields and, consequently, the overall neutrino fluxes. This optimisation process would target two different objectives: (1) improvement of the target performance and (2) further improvement of the optics design to increase as much as possible the accepted phase space, including the acceptance through the final spectrometer.

Particularly for the first part, the target geometry could be further optimised, including e.g. segmentation that would possibly increase the pion yield. Also, a more complete optimisation process could be carried out, eventually considering other materials and graphite densities available in the market. This process should also include thermo-mechanical calculations to evaluate in depth the target station exact geometry and target life. Regarding the second point, various paths could be explored leading to an overall optimisation of the optics and accepted phase space, in a similar manner as in Ref. [77]. As indicated from Fig. 11, the vertical 140 mm aperture of the bending magnets composing the first and second achromat, strongly limits the $\pi^\pm$ accepted phase space. While a very strong field, and therefore small gap, is needed to separate the two charges at the momentum selection stage in the first achromat, the constraint on the aperture could be relaxed at the meson tracking station, where the resolution of the spectrometer is enough to measure $\pi^\pm$ momentum with smaller displacements (for a $< 1\%$ momentum resolution a minimum displacement from the beam axis of 5 cm is required, compared to the ≈ 12 cm considered in this study). This would most likely improve also the $\pi^\pm$ beam size and divergence, without exceeding the limits of the tagger maximum accepted rate. Another element affecting the phase space and momentum acceptance is the collimator. Besides momentum selecting the $\pi^\pm$ beams, the purpose of this beamline element is to act as a dump for the primary proton beam. Our conceptual dump (comprising approximately 30 nuclear interaction lengths) is very effective in absorbing the primary beam and in cleaning the produced low energy secondaries from being

transported downstream, however, other designs (*e.g* with asymmetric or tapered apertures) and a shorter length could be foreseen, finding the best compromise in the signal to background ratio.

Finally, the analysis of the background and its implications on the performances of the tagger have not been treated in the current study but are fundamental to have a complete picture of the proposed beamline capabilities. Some preliminary simulations have been done to estimate the main sources of background, which are mainly muons produced by the interaction of the primary proton beam with the dump and neutrinos produced both in the target and in the dump. While the background neutrinos are mostly emitted at large angles and are not likely to reach the far detector, the muon background could be concerning both for the tagger, in terms of maximum charged particle rate, and for the neutrino flux generated by background muons and reaching the far detector. Preliminary results show a muon background of ≈ 0.015 muons/primary in the momentum range $p < 14 \, \mathrm{GeV}/c$ for a central momentum of $12 \, \mathrm{GeV}/c$, compared to the ≈ 0.053 pions/primary $\pi^\pm$ signal. Further studies will be conducted in the future to better understand the effects of this background on the overall performance of the beamline and on the precision on the measurement of the neutrino flux. Similarly, the background arising from the decays of muons from $\pi^\pm \to \mu^\pm \overset{\frown}{\nu}_\mu$ will need a dedicated study.

In this work, we have performed a first comprehensive study towards a long-baseline tagged neutrino beam using the NuTag technique. More studies are needed in the future in order to better understand the sources of background along with the inherent Monte Carlo uncertainties that need to be looked at in more detail, including a respective analysis of fitting benchmarked data.

Data Availability Statement This manuscript has no associated data. [Authors' comment: The data generated through Monte Carlo simulations and analysed during the current study are available from the corresponding author and N. Charitonidis (CERN) on justified/reasonable request.].

Code Availability Statement Code/software will be made available on reasonable request. [Authors' comment: The code/software generated during the current study is available from the corresponding author and N. Charitonidis (CERN) on justified/reasonable request.].

References

1. M. Perrin-Terrin, Neutrino tagging: a new tool for accelerator based neutrino experiments. Eur. Phys. J. C **82**(5), 465 (2022). https://doi.org/10.1140/epjc/s10052-022-10397-8

2. A. Branca, G. Brunetti, A. Longhin, M. Martini, F. Pupilli, F. Terranova, A new generation of neutrino cross section experiments: challenges and opportunities. Symmetry **13**(9), 1625 (2021). https://doi.org/10.3390/sym13091625

3. S.S. Chatterjee, P.S.B. Dev, P.A.N. Machado, Impact of improved energy resolution on DUNE sensitivity to neutrino non-standard interactions. J. High Energy Phys. **08**, 163 (2021). https://doi.org/10.1007/JHEP08(2021)163

4. V. De Romeri, E. Fernandez-Martinez, M. Sorel, Neutrino oscillations at DUNE with improved energy reconstruction. J. High Energy Phys. **09**, 030 (2016). https://doi.org/10.1007/JHEP09(2016)030

5. M. Sajjad Athar, A. Fatima, S. Singh, Neutrinos and their interactions with matter. Prog. Part. Nucl. Phys. **129**, 104019 (2023). https://doi.org/10.1016/j.ppnp.2022.104019

6. G. Knoll, *Radiation Detection and Measurement* (Wiley, New York, 2000)

7. A. Friedland, S.W. Li, Understanding the energy resolution of liquid argon neutrino detectors. Phys. Rev. D **99**(3), 036009 (2019). https://doi.org/10.1103/PhysRevD.99.036009

8. Hyper-Kamiokande Proto-Collaboration, K. Abe, K. Abe, H. Aihara, A. Aimi, R. Akutsu, C. Andreopoulos, I. Anghel, L.H.V. Anthony, M. Antonova, Y. Ashida, V. Aushev, M. Barbi, G.J. Barker, G. Barr, P. Beltrame, V. Berardi, M. Bergevin, S. Berkman, L. Berns, (...), S. Zsoldos, Hyper-Kamiokande Design Report (2018). https://doi.org/10.48550/arXiv.1805.04163

9. E.S. Group, 2020 Update of the European Strategy for Particle Physics (Brochure), Tech. rep., CERN, Geneva (2020). https://doi.org/10.17181/CERN.JSC6.W89E

10. B. Abi, R. Acciarri, M.A. Acero, G. Adamov, M. Adinolfi, Z. Ahmad, J. Ahmeed, T. Alion, S. Alonso Monsalve, C. Alt, J. Anderson, C. Andreopoulos, M.P. Andrews, F. Andrianala, S. Andriga, A. Ankowski, M. Antonova, S. Antusch, A. Aranda-Fernandez, (...), R. Zwaska, Long-baseline neutrino oscillation physics potential of the DUNE experiment. Eur. Phys. J. C **80**(10), 978 (2020). https://doi.org/10.1140/epjc/s10052-020-08456-z

11. B. Pontecorvo, Tagging direct neutrinos: a first step to neutrino tagging. Lett. Nuovo Cim. **25**, 257–259 (1979). https://doi.org/10.1007/BF02813638

12. I.P. Nedyalkov, Single spectrometer station for neutrino tagging (1984). http://inis.jinr.ru/sl/NTBLIB/JINR-E1-84-515.pdf

13. V. Kaftanov, On tagging neutrinos in a high-band beam (1979)

14. L.N. Hand, A Study of 40-90 GeV Neutrino Interactions Using a Tagged Neutrino Beam (1969)

15. A.A. Boikov, S.P. Denisov, A.V. Erokhin, S.A. Mukhin, A.A. Spiridonov, V.P. Zhigunov, Tagged muon neutrino beam characteristics (1980)

16. G. Bohm, Project of a tagged neutrino facility at Serpukhov (1987)

17. R.H. Bernstein, F. Borcherding, D. Jovanovic, M.J. Lamm, F. Vanucci, A Proposal for a Neutrino Oscillation Experiment in a Tagged Neutrino Line (1990)

18. R.H. Bernstein, Neutrino Physics in a Tagged Neutrino Beam, in *Conference on New Directions in Neutrino Physics at Fermilab* (1989). https://lss.fnal.gov/archive/1989/conf/Conf-89-034.pdf

19. V.B. Anikeev, S.V. Belikov, S.N. Gurzhiev, A.G. Denisov, S.P. Denisov, N.N. Fedjakin, V.I. Kochetkov, V.M. Korablev, V.I. Koreshev, V.V. Lipaev, S.V. Los, V.N. Mikhailin, A.M. Rybin, A.N. Sytin, A.G. Bogdanov, T.M. Kirina, R.P. Kokoulin, M.A. Reznikov, A. A. Petrukhin, (...), F. Martelli, Use of the big liquid argon spectrometer BARS for neutrino and cosmic ray studies. Nucl. Instrum. Methods Phys. Res. A Accel. Spectrom. Detect. Assoc. Equip. **419**, 596–601 (1998). https://doi.org/10.1016/S0168-9002(98)00837-7

20. G.A. Rinella, D.A. Feito, R. Arcidiacono, C. Biino, S. Bonacini, A. Ceccucci, S. Chiozzi, E.C. Gil, A.C. Ramusino, H. Danielsson, J. Degrange, M. Fiorini, L. Federici, E. Gamberini, A. Gianoli, J. Kaplon, A. Kleimenova, A. Kluge, R. Malaguti, (...), H. Wahl, The NA62 GigaTracKer: a low mass high intensity beam 4D tracker with 65 ps time resolution on tracks. J. Instrum. **14**, P07010 (2019). https://doi.org/10.1088/1748-0221/14/07/P07010

21. A. Lai, A system approach towards future trackers at high luminosity colliders: the TIMESPOT Project, in *2018 IEEE Nuclear Science Symposium and Medical Imaging Conference Proceedings (NSS/MIC)*. IEEE, Sydney, pp. 1–3 (2018). https://doi.org/10.1109/NSSMIC.2018.8824310

22. ECFA Detector R&D Roadmap Process Group, The 2021 ECFA detector research and development roadmap, Tech. rep., CERN, Geneva (2020). https://doi.org/10.17181/CERN.XDPL.W2EX

23. A. Lai, A. Lampis, 10ps timing with 3D trench silicon pixel sensors, talk given at "23rd IWORID", Riva del Garda, July 2022. (2022). https://indico.cern.ch/event/1120714/contributions/4867208/

24. S. Adrián-Martínez, M. Ageron, F. Aharonian, S. Aiello, A. Albert, F. Ameli, E. Anassontzis, M. Andre, G. Androulakis, M. Anghinolfi, G. Anton, M. Ardid, T. Avgitas, G. Barbarino, E. Barbarito, B. Baret, B. Belhorma, A. Belias, (...), J. Zúñiga, Letter of intent for KM3NeT 2.0. J. Phys. G Nucl. Part. Phys. **43**(8), 084001 (2016). https://doi.org/10.1088/0954-3899/43/8/084001

25. S. Aiello, A. Albert, S. Alves Garre, Z. Aly, A. Ambrosone, F. Ameli, M. Andre, G. Androulakis, M. Anghinolfi, M. Anguita, G. Anton, M. Ardid, S. Ardid, J. Aublin, C. Bagatelas, B. Baret, S. Basegmez du Pree, M. Bendahman, F. Benfenati, (...), N. Zywucka, Determining the neutrino mass ordering and oscillation parameters with KM3NeT/ORCA. Eur. Phys. J. C **82**(1), 26 (2022). https://doi.org/10.1140/epjc/s10052-021-09893-0

26. P.D. Group, R.L. Workman, V.D. Burkert, V. Crede, E. Klempt, U. Thoma, L. Tiator, K. Agashe, G. Aielli, B.C. Allanach, C. Amsler, M. Antonelli, E.C. Aschenauer, D.M. Asner, H. Baer, S. Banerjee, R.M. Barnett, L. Baudis, C.W. Bauer, J. Beatty, (...), P.A. Zyla, Review of particle physics. Prog. Theor. Exp. Phys. **2022**, 083C01 (2022). https://doi.org/10.1093/ptep/ptac097

27. A.V. Akindinov, E.G. Anassontzis, G. Anton, M. Ardid, J. Aublin, B. Baret, V. Bertin, S. Bourret, C. Bozza, M. Bruchner, R. Bruijn, J. Brunner, M. Chabab, N. Chau, A.S. Chepurnov, M. Colomer Molla, P. Coyle, A. Creusot, G. de Wasseige, J. Zúñiga, Letter of interest for a neutrino beam from Protvino to KM3NeT/ORCA. Eur. Phys. J. C **79**(9), 758 (2019). https://doi.org/10.1140/epjc/s10052-019-7259-5

28. E. Leonora, The digital optical module of KM3NeT. J. Phys. Conf. Ser. **1056**(1), 012031 (2018). https://doi.org/10.1088/1742-6596/1056/1/012031

29. J. Hofestädt, M. Bruchner, T. Eberl, Super-ORCA: measuring the leptonic CP-phase with Atmospheric Neutrinos and Beam Neutrinos. PoS Proc. Sci. **ICRC2019**, 911 (2020). https://doi.org/10.22323/1.358.0911

30. A.E. Ball, S. Katsanevas, N. Vassilopoulos, Design studies for a long base-line neutrino beam (1995). https://cds.cern.ch/record/287643

31. A.E. Ball, A. Braem, L. Camilleri, A. Catinaccio, G. Chelkov, F. Dydak, A. Elagin, P.K. Frandsen, M. Gostkin, A. Grant, A. Guskov, C. Joram, Z. Krumshteyn, H. Müller, H. Postema, M. Price, T. Rovelli, D. Schinzel, J. Séguinot, G. Valenti, (...), A. Zhemchugov, C2GT: intercepting CERN neutrinos to Gran Sasso in the Gulf of Taranto to measure Theta(13). Eur. Phys. J. C **49**, 1117–1142 (2007). https://doi.org/10.1140/epjc/s10052-006-0193-3

32. C. Vallee, Pacific Neutrinos: Towards a High Precision Measurement of CP Violation? (2016). https://doi.org/10.48550/arXiv.1610.08655

33. J. Coelho, OscProb Neutrino Oscillation Calculator. https://github.com/joaoabcoelho/OscProb

34. S.P. Mikheyev, A.Y. Smirnov, Resonance amplification of oscillations in matter and spectroscopy of solar neutrinos. Sov. J. Nucl. Phys. **42**, 913–917 (1985)

35. L. Wolfenstein, Neutrino oscillations in matter. Phys. Rev. D **17**(9), 2369–2374 (1978). https://doi.org/10.1103/physrevd.17.2369

36. C. Franzinetti (ed.), Informal Conference on Experimental Neutrino Physic. CERN, Geneva (1965). https://doi.org/10.5170/CERN-1965-032

37. S.E. Kopp, Accelerator neutrino beams. Phys. Rep. **439**(3), 101–159 (2007). https://doi.org/10.1016/j.physrep.2006.11.004

38. N. Charitonidis, A. Longhin, M. Pari, E.G. Parozzi, F. Terranova, Design and diagnostics of high-precision accelerator neutrino beams. Appl. Sci. (2021). https://doi.org/10.3390/app11041644

39. U. Dore, P. Loverre, L. Ludovici, History of accelerator neutrino beams. Eur. Phys. J. H **44**, 271–305 (2019). https://doi.org/10.1140/epjh/e2019-90032-x

40. G. Acquistapace, V.P. Falaleev, J. M. Maugain, G. Olesen, S. Rangod, J. Zaslavsky, The West Area neutrino facility for CHORUS and NOMAD experiments (94-97 operation), Tech. rep., CERN, Geneva (1995). https://cds.cern.ch/record/286076

41. S. Choubey, R. Gandhi, S. Goswami, J. Berg, R. Fernow, J. Gallardo, R. Gupta, H. Kirk, N. Simos, N. Souchlas, M. Ellis, P. Kyberd, E. Benedetto, E. Fernandez-Martinez, I. Efthymiopoulos, R. Garoby, S. Gilardoni, M. Martini, G. Prior, (...), W. Winter, International Design Study for the Neutrino Factory, Interim Design Report (2011). arXiv:1112.2853

42. O. Caretta, P. Loveridge, J. O'Dell, T. Davenne, M. Fitton, A. Atherton, C. Densham, N. Charitonidis, I. Efthymiopoulos, A. Fabich, M. Guinchard, L.J. Lacny, B. Lindstrom, Proton beam induced dynamics of tungsten granules. Phys. Rev. Accel. Beams **21**, 033401 (2018). https://doi.org/10.1103/PhysRevAccelBeams.21.033401

43. H.-J. Cai, H. Jia, X. Qi, P. Lin, S. Zhang, Y. Tian, Y. Qin, X. Zhang, L. Yang, Y. He, Beam-target configurations and robustness performance of the tungsten granular flow spallation target for an accelerator-driven sub-critical system. Nucl. Eng. Technol. **54**(7), 2650–2659 (2022). https://doi.org/10.1016/j.net.2022.01.022

44. M.I. Radaideh, H. Tran, L. Lin, H. Jiang, D. Winder, S. Gorti, G. Zhang, J. Mach, S. Cousineau, Model calibration of the liquid mercury spallation target using evolutionary neural networks and sparse polynomial expansions. Nucl. Instrum. Methods Phys. Res. B Beam Interact. Mater. At. **525**, 41–54 (2022). https://doi.org/10.1016/j.nimb.2022.06.001

45. N. Simos, E. Quaranta, N. Charitonidis, D. Sprouster, Z. Zhong, S. Ghose, Z. Kotsina, R. Assmann, S. Redaelli, A. Bertarelli, A. Ryazanov, Radiation damage of a two-dimensional carbon fiber composite (CFC). Carbon Trends **3**, 100028 (2021). https://doi.org/10.1016/j.cartre.2021.100028

46. A. Ichikawa, Design concept of the magnetic horn system for the T2K neutrino beam. Nucl. Instrum. Methods Phys. Res. A Accel. Spectrom. Detect. Assoc. Equip. **690**, 27–33 (2012). https://doi.org/10.1016/j.nima.2012.06.045

47. A. Liu, A. Bross, D. Neuffer, Optimization of the magnetic horn for the nuSTORM non-conventional neutrino beam using the genetic algorithm. Nucl. Instrum. Methods Phys. Res. A Accel. Spectrom. Detect. Assoc. Equip. **794**, 200–205 (2015). https://doi.org/10.1016/j.nima.2015.05.035

48. S. van der Meer, A directive device for charged particles and its use in an enhanced neutrino beam, CERN Yellow Reports: Monographs. CERN, Geneva (1961). https://doi.org/10.5170/CERN-1961-007

49. N. Charitonidis, I. Efthymiopoulos, Low energy tertiary beam line design for the cern neutrino platform project. Phys. Rev. Accel. Beams **20**, 111001 (2017). https://doi.org/10.1103/PhysRevAccelBeams.20.111001

50. A.C. Booth, N. Charitonidis, P. Chatzidaki, Y. Karyotakis, E. Nowak, I. Ortega-Ruiz, M. Rosenthal, P. Sala, Particle production, transport, and identification in the regime of $1 - 7\mathrm{GeV}/c$. Phys. Rev. Accel. Beams **22**, 061003 (2019). https://doi.org/10.1103/PhysRevAccelBeams.22.061003

51. B. Abi, A.A. Abud, R. Acciarri, M. Acero, G. Adamov, M. Adamowski, D. Adams, P. Adrien, M. Adinolfi, Z. Ahmad, J. Ahmed, T. Alion, S. A. Monsalve, C. Alt, J. Anderson, C. Andreopoulos, M. Andrews, F. Andrianala, S. Andringa, (...), R. Zwaska, First results on ProtoDUNE-SP liquid argon time projection chamber performance from a beam test at the CERN Neutrino Platform. J. Instrum. **15**(12), P12004 (2020). https://doi.org/10.1088/1748-0221/15/12/P12004

52. H. Wiedemann, *Particle Accelerator Physics* (Springer, Cham, 2015)

53. H.W. Atherton, C. Bovet, N.T. Doble, L. Piemontese, A. Placci, M. Placidi, D.E. Plane, M. Reinharz, E. Rossa, G. Von Holtey, Precise measurements of particle production by 400 GeV/c protons on beryllium targets, CERN Yellow Reports: Monographs. CERN, Geneva (1980). https://doi.org/10.5170/CERN-1980-007

54. L. Gatignon,Magnets Kit for the Experimental Areas of the 'CERN PS/SPS complex, Tech. rep., CERN, Geneva (1991). https://cds.cern.ch/record/711814

55. K. Brown, D. Carey, C. Iselin, F. Rothacker, TRANSPORT: A Computer Program for Designing Charged Particle Beam Transport Systems, Tech. Rep. CERN80-04, CERN Super Proton Synchrotron Division, CERN, Geneva (1980). https://cds.cern.ch/record/133647

56. H. Grote, F. Schmidt, MAD-X—an upgrade from MAD8, in *Proceedings of the 2003 Particle Accelerator Conference*, vol. 5, pp. 3497–3499 (2003). https://doi.org/10.1109/PAC.2003.1289960

57. C. Ahdida, D. Bozzato, D. Calzolari, F. Cerutti, N. Charitonidis, A. Cimmino, A. Coronetti, G.L. D'Alessandro, A. Donadon Servelle, L.S. Esposito, R. Froeschl, R. García Alía, A. Gerbershagen, S. Gilardoni, D. Horváth, G. Hugo, A. Infantino, V. Kouskoura, A. Lechner, (...), M. Widorski, New capabilities of the FLUKA multi-purpose code. Front. Phys. (2022). https://doi.org/10.3389/fphy.2021.788253

58. G. Battistoni, T. Boehlen, P.C.F. Cerutti, L. Esposito, A. Fassò, A. Ferrari, A. Lechner, A. Empl, A. Mairani, A. Mereghetti, P.G. Ortega, J. Ranft, S. Roesler, P. Sala, G.S.V. Vlachoudis, Overview of the FLUKA code. Ann. Nucl. Energy **82**, 10–18 (2015)

59. E. Gschwendtner, L. Bruno, K. Elsener, A. Ferrari, A. Guglielmi, M. Meddahi, A. Pardons, S. Rangod, P. Sala, Design and Performance of the CNGS Secondary Beam Line, Tech. rep., CERN, Geneva (2007). https://cds.cern.ch/record/1053097

60. L. Bruno, I. Efthymiopoulos, The CNGS Target—Explained (2011). http://operaweb.lngs.infn.it/Opera/publicnotes/note138.pdf

61. T. Jyoti, Study of a New Target Design with an Additional Horn for NuMI Beam (2017). https://doi.org/10.48550/arXiv.1710.03699

62. P. Adamson, K. Anderson, M. Andrews, R. Andrews, I. Anghel, D. Augustine, A. Aurisano, S. Avvakumov, D. Ayres, B. Baller, B. Barish, G. Barr, W. Barrett, R. Bernstein, J. Biggs, M. Bishai, A. Blake, V. Bocean, G. Bock, (...), R. Zwaska, The NuMI neutrino beam. Nucl. Instrum. Methods Phys. Res. A Accel. Spectrom. Detect. Assoc. Equip. **806**, 279–306 (2016). https://doi.org/10.1016/j.nima.2015.08.063

63. K. Abe, , N. Abgrall, H. Aihara, Y. Ajima, J. Albert, D. Allan, P.-A. Amaudruz, C. Andreopoulos, B. Andrieu, M. Anerella, C. Angelsen, S. Aoki, O. Araoka, J. Argyriades, A. Ariga, T. Ariga, S. Assylbekov, J. de André, D. Autiero, (...), J. Zmuda, The T2K experiment. Nucl. Instrum. Methods Phys. Res. A Accel. Spectrom. Detect. Assoc. Equip. **659**(1), 106–135 (2011). https://doi.org/10.1016/j.nima.2011.06.067

64. F. Acerbi, I. Angelis, L. Bomben, M. Bonesini, F. Bramati, A. Branca, C. Brizzolari, G. Brunetti, M. Calviani, S. Capelli, S. Carturan, M. Catanesi, S. Cecchini, N. Charitonidis, F. Cindolo, G. Cogo, G. Collazuol, F. Dal Corso, C. Delogu, (...), L. Votano, Design and performance of the ENUBET monitored neutrino beam. Eur. Phys. J. C **83**(10), 964 (2023). https://doi.org/10.1140/epjc/s10052-023-12116-3

65. V. Vlachoudis,FLAIR: A Powerful But User Friendly Graphical Interface to FLUKA, in *Proc. Int. Conf. on Mathematics, Computational Methods and Reactor Physics* (2009). https://cds.cern.ch/record/2749540

66. M. Rosenthal, N. Charitonidis, P. Chatzidaki, R. Margraf, H. Wilkens, F. Bergsma, P.-A. Giudici, Magnetic Field Measurements of the GOLIATH Magnet in EHN1 (2018). https://cds.cern.ch/record/2310483

67. M. Morpurgo, A large superconducting dipole cooled by forced circulation of two phase helium. Cryogenics **19**(7), 411–414 (1979). https://doi.org/10.1016/0011-2275(79)90126-7

68. E.C. Gil, E.M. Albarrán, E. Minucci, G. Nüssle, S. Padolski, P. Petrov, N. Szilasi, B. Velghe, G. Georgiev, V. Kozhuharov, L. Litov, T. Husek, K. Kampf, M. Zamkovsky, R. Aliberti, K.H. Geib, G. Khoriauli, K. Kleinknecht, J. Kunze, (...), R. Winston, The beam and detector of the NA62 experiment at CERN. J. Instrum. **12**(05), P05025 (2017). https://doi.org/10.1088/1748-0221/12/05/P05025

69. HIKE Collaboration, High Intensity Kaon Experiments (HIKE) at the CERN SPS Proposal for Phases 1 and 2, Tech. rep., CERN (2023). https://doi.org/10.48550/ARXIV.2311.08231

70. F. Hahn, F. Ambrosino, A. Ceccucci, H. Danielsson, N. Doble, F. Fantechi, A. Kluge, C. Lazzeroni, M. Lenti, G. Ruggiero, M. Sozzi, P. Valente, R. Wanke, NA62: Technical Design Document, Tech. rep., CERN, Geneva (2010). https://cds.cern.ch/record/1404985

71. LHCb Collaboration, Framework TDR for the LHCb Upgrade II: Opportunities in flavour physics, and beyond, in the HL-LHC era, Tech. rep., CERN, Geneva (2021). https://cds.cern.ch/record/2776420

72. K.L. Brown, First- and second-order matrix theory for the design of beam transport systems and charged particle spectrometers., Tech. rep., SLAC National Accelerator Lab., Menlo Park, CA (United States) (1971). https://doi.org/10.2172/4742148

73. M. Tanabashi, K. Hagiwara, K. Hikasa, K. Nakamura, Y. Sumino, F. Takahashi, J. Tanaka, K. Agashe, G. Aielli, C. Amsler, M. Antonelli, D.M. Asner, H. Baer, S. Banerjee, R.M. Barnett, T. Basaglia, C.W. Bauer, J.J. Beatty, V.I. Belousov, (...), P. Schaffner, Review of particle physics. Phys. Rev. D **98**, 030001 (2018). https://doi.org/10.1103/PhysRevD.98.030001

74. F.E. James, Monte Carlo phase space, CERN Academic Training Lecture, CERN. Geneva (1968). https://doi.org/10.5170/CERN-1968-015

75. A. Alekou, E. Baussan, A.K. Bhattacharyya, N.B. Kraljevic, M. Blennow, M. Bogomilov, B. Bolling, E. Bouquerel, O. Buchan, A. Burgman, C.J. Carlile, J. Cederkall, P. Christiansen, M. Collins, E.C. Morales, P. Cupiał, L. D'Alessi, H. Danared, D. Dancila, (...), Y. Zou, The European Spallation Source neutrino Super Beam Conceptual Design Report. Eur. Phys. J. Spec. Top. **231**(21), 3779–3955 (2022). https://doi.org/10.1140/epjs/s11734-022-00664-w

76. A. Bogacz, V. Brdar, A. Bross, A. de Gouvêa, J.-P. Delahaye, P. Huber, M. Hostert, K.J. Kelly, K. Long, M. Palmer, J. Pasternak, C. Rogers, Z. Tabrizi, The Physics Case for a Neutrino Factory (2022). https://doi.org/10.48550/ARXIV.2203.08094

77. C. Mussolini, P. Burrows, N. Charitonidis, Y. Nagai, E. Zimmerman, Design of a Very Low Energy Beamline for NA61/SHINE, in *Proc. IPAC'21, no. 12 in International Particle Accelerator Conference*. JACoW Publishing, Geneva, pp. 4017–4020 (2021). https://doi.org/10.18429/JACoW-IPAC2021-THPAB130